CANCER

KIX domain determines a selective tumor-promoting role for EP300 and its vulnerability in small cell lung cancer

Kee-Beom Kim[1], Ashish Kabra[2], Dong-Wook Kim[1], Yongming Xue[3], Yuanjian Huang[4], Pei-Chi Hou[1], Yunpeng Zhou[2]†, Leilani J. Miranda[1], Jae-Il Park[4], Xiaobing Shi[5], Timothy P. Bender[1,6], John H. Bushweller[2]*‡, Kwon-Sik Park[1]*‡

EP300, a transcription coactivator important in proliferation and differentiation, is frequently mutated in diverse cancer types, including small cell lung cancer (SCLC). While these mutations are thought to result in loss of EP300 function, the impact on tumorigenesis remains largely unknown. Here, we demonstrate that EP300 mutants lacking acetyltransferase domain accelerate tumor development in mouse models of SCLC. However, unexpectedly, complete *Ep300* knockout suppresses SCLC development and proliferation. Dissection of EP300 domains identified kinase inducible domain-interacting (KIX) domain, specifically its interaction with transcription factors including MYB, as the determinant of protumorigenic activity. Ala^{627} in EP300 KIX results in a higher protein-binding affinity than Asp^{647} at the equivalent position in CREBBP KIX, underlying the selectivity of KIX-binding partners for EP300. Blockade of KIX-mediated interactions inhibits SCLC development in mice and cell growth. This study unravels domain-specific roles for EP300 in SCLC and unique vulnerability of the EP300 KIX domain for therapeutic intervention.

INTRODUCTION

Cancers are often initiated and driven by loss-of-function mutations in transcription coactivator and chromatin modifiers that play tumor suppressor roles. However, restoration of these lost tumor suppressor functions has proven considerably more challenging than inhibiting oncogenic drivers, and viable targets downstream of the mutations often remain elusive. This fundamental problem is particularly relevant to recurrent mutations in *EP300* and *CREBBP* that encode closely related transcription coactivators (hence frequently referred *EP300/CREBBP*).

EP300 (E1A binding protein p300) and CREBBP (cAMP response element biding (CREB)-binding protein) are ubiquitously expressed and control a number of fundamental biological processes including proliferation and differentiation through the actions of paralogous domains, including transcriptional adaptor zinc-binding (TAZ), kinase-inducible domain–interacting (KIX), bromodomain (BRD), and histone acetyltransferase (HAT) (*1*). This versatility of EP300/CREBBP renders them frequent targets of various oncogenic insults. Oncogenic viral proteins such as adenovirus E1A and HPV E7 bind to EP300/CREBBP coopt the coactivator functions to promote cellular transformation (*2*, *3*). Inactivating mutations in *EP300/CREBBP* are thought to promote numerous cancer types including lymphoma, leukemia, bladder cancer, and SCLC (*4*–*10*). Recent studies demonstrated that loss of CREBBP HAT function reduces expression of various tumor suppressor genes and promotes tumor development and progression in lymphoma and small cell lung cancer (SCLC) (*11*–*14*). Inhibitors of histone deacetylase (HDAC) rescue the expression of tumor suppressor genes and inhibit tumor development to some extent (*13*, *14*). However, the limited effect of HDAC inhibition suggests a broader scope of molecular alterations caused by EP300/CREBBP mutations, which remain poorly understood. Meanwhile, little has been elucidated about potential roles of TAZ, KIX, and BRD domains in tumorigenesis. These domains mediate diverse interactions among a network of proteins to regulate numerous biological processes, making it difficult to parse roles of each domain in cell homeostasis and pathogenesis. Furthermore, while in vivo evidence indicates nonoverlapping functions of EP300 and CREBBP, significant structural similarities between their functional domains make it difficult to determine the individual contributions of each of the proteins to tumorigenesis, given the numerous ways in which these proteins interact with binding partners and compensate for each other (*15*). To begin to address these problems, it is necessary to develop models that better recapitulate the mutations in the transcription coactivators identified in the patient tumors. This study is focused on SCLC as it is a relevant disease of immense clinical importance.

SCLC accounts for approximately 13% of lung cancer diagnosis yet remains an exceptionally lethal disease (*16*). Unlike lung adenocarcinoma carrying actionable drivers such as epidermal growth factor receptor and KRAS (Kirsten rat sarcoma viral oncogene homolog), SCLC is primarily driven by loss of tumor suppressors with near-universal inactivation of both RB and P53 and frequent loss of other putative tumor suppressors among which missense, truncating, and deletion mutations in *EP300* and *CREBBP* were detected in 5 to 13% and 15 to 17% of SCLC patient tumors, respectively (*4*–*7*). While these loss-of-function mutations in *EP300* and *CREBBP* themselves appear undruggable, understanding of how they drive SCLC development and progression remains very limited, which further hinders efforts to develop strategies for tumor prevention and intervention (*16*).

[1]Department of Microbiology, Immunology, and Cancer Biology, University of Virginia, Charlottesville, VA 22908, USA. [2]Department of Molecular Physiology and Biological Physics, University of Virginia, Charlottesville, VA 22908, USA. [3]Department of Epigenetics and Molecular Carcinogenesis, MD Anderson Cancer Center, Houston, TX 77030, USA. [4]Department of Experimental Radiation Oncology, MD Anderson Cancer Center, Houston, TX 77030, USA. [5]Department of Epigenetics, Van Andel Research Institute, Grand Rapids, MI 49503, USA. [6]Beirne B. Carter Center for Immunology Research, University of Virginia, Charlottesville, VA 22908, USA.
*Corresponding author. Email: jhb4v@virginia.edu (J.H.B.); kp5an@virginia.edu (K.-S.P.)
†Present address: Computational and Structural Chemistry, Merck & Co. Inc., 2000 Galloping Hill Road, Kenilworth, NJ 07033, USA.
‡These authors contributed equally to this work.

In this study, we tested whether EP300 loss-of-function promotes SCLC development and growth. Unexpectedly, the results from SCLC GEMM (genetically engineered mouse model) and cancer cells indicate a tumor-promoting role for EP300 KIX domain, which is distinct from a tumor-suppressive role of HAT domain. We then determined how EP300 KIX exerts the protumorigenic role and how its action differs from CREBBP KIX. Biochemical analysis showed that an alanine-versus-aspartate difference in the EP300 and CREBBP KIX domains defines differential binding affinities of the proteins to KIX-binding partners. Specifically, Ala^{627} in EP300 KIX domain is crucial for interaction with tumor-promoting transcription factors (TFs). Furthermore, we asked whether inhibition of EP300 KIX-mediated protein interactions results in the same tumor-suppressive impact of inactivating the KIX domain. Biochemical and chemical inhibition of the interactions between the KIX domain and its binding partners selectively suppresses SCLC cell proliferation and tumor development in vivo. These findings define the EP300 KIX domain as a molecular vulnerability for therapeutic intervention in SCLC, an exceptionally lethal lung cancer that lacks readily actionable oncogenic drivers for targeted therapies. The biochemical differences between the EP300 and CREBBP KIX domains, determined by a single–amino acid difference, may provide critical insight into the underlying mechanism of the discrete roles that EP300 and CREBBP play in development and disease.

RESULTS

EP300 knockout suppresses SCLC

The recurrent mutations (approximately 13%) observed in the *EP300* gene in human SCLC tumors are largely thought to be loss-of-function mutations, suggesting that EP300 is a tumor suppressor in SCLC. Accordingly, loss-of-function studies in cell lines and in mice previously suggested that the EP300-related protein CREBBP acts as a tumor suppressor in SCLC (*5*, *6*). To determine the role of EP300 in SCLC development in vivo, we conditionally deleted *Ep300* in two strains of genetically engineered mouse models of SCLC: *Rb1*/*Trp53*/*Rbl2*-mutant (*RPR2*) and *Rb1*/*Trp53*/*Myc*-mutant (*RPM*) mice. In addition to deleting *Rb1* and *Trp53*, introduction of adenovirus Cre results in deletion of *Rbl2* in *RPR2* mice and induction of an oncogenic form of MYC (MYC^{T58A}) in *RPM* mice (Fig. 1A). These two genetic manipulations account for significant portions of recurrent SCLC alterations and were shown to result in development of lung tumors resembling the two major molecular subtypes of human SCLC that are defined by ASCL1 (achaete-scute complex-like 1) and NEUROD1 (neuronal differentiation 1) and unique therapeutic vulnerabilities (*17*–*20*). We induced lung tumor via intratracheal infection of Ad–calcitonin-gene related peptide (CGRP)–Cre that expresses Cre under the control of a neuroendocrine-specific CGRP promoter (*21*) and, 7 months later, observed development of nodular lung tumors in $Ep300^{+/+}$ *RPR2* mice as expected; $Ep300^{\Delta/\Delta}$ *RPR2* mice, however, developed only small lesions (Fig. 1B). The small lesions and tumors from mice of both genotypes consisted of small cells with scanty cytoplasm that stained for CGRP, indicative of SCLC (fig. S1A). Likewise, 9 weeks after infection of Ad-CGRP-Cre, mice with *Ep300* deletion ($Ep300^{\Delta/\Delta}$ *RPM*) developed fewer and smaller lesions in the lung than mice with intact EP300 ($Ep300^{+/+}$ *RPM*) (Fig. 1C and fig. S1B). Lesions in $Ep300^{\Delta/\Delta}$ *RPR2* and $Ep300^{\Delta/\Delta}$ *RPM* mice contained a smaller proportion of cells stained positive for a proliferation marker, phosphorylated histone H3 (pHH3), than tumors in $Ep300^{+/+}$ *RPR2* and $Ep300^{+/+}$ *RPM* mice (Fig. 1, D and E).

Next, we determined whether *Ep300* is also required for proliferation of SCLC cells. We performed CRISPR-mediated knockout (KO) of EP300 in tumor cells derived from *RP* (*Rb1*/*Trp53*-mutant) and *RPR2* mice and in human SCLC lines (fig. S2, A to D). The EP300 KO cells significantly inhibited proliferation compared with control cells expressing a nontargeting guide RNA (gRNA) (Fig. 1, F and G, and fig. S2D). Notably, KO of *Crebbp*, the structural and functional homolog of *Ep300*, had either insignificant or modest effects, and neither *Ep300* nor *Crebbp* KO significantly affected the proliferation of non-SCLCs (NSCLCs; A549 and H1299) and human bronchial epithelial cells (Fig. 1, F and G, and fig. S2E). Thus, while EP300 is thought to be a tumor suppressor in SCLC, complete EP300 loss of function reveals a unique requirement for EP300 in SCLC development and cell proliferation. These data further suggest that EP300 and CREBBP may have nonoverlapping roles.

Inactivation of EP300 HAT promotes SCLC

EP300 is expressed in SCLC patient tumors, where it frequently harbors mutations in the HAT domain (Fig. 2A) (*5*). We thus wondered whether the phenotypes of mice would be different if, instead complete loss of function, we were able to model the patient mutations. We developed an adenovirus CRISPR-Cre hybrid vector (Ad-gEp300/Cas9-Cre) that expresses Cre recombinase, deleting the floxed alleles of *Rb1*, *Trp53*, and *Rbl2*, as well as Cas9 and a gRNA against *Ep300* exon 27 encoding a part of the HAT domain (Fig. 2B). This new approach facilitates testing physiological impact of candidate mutations on SCLC development in vivo without generating new mutant strains and time-consuming genetic crosses. Ad-gLacZ/Cas9-Cre was used as a control that expresses gRNA against a bacterial gene *LacZ*. After 7 months, *RPR2* mice infected with Ad-gEp300/Cas9-Cre developed larger lung tumor with a higher proportion of pHH3-positive cells than small lesions in mice infected with Ad-gLacZ/Cas9-Cre (Fig. 2, C and D, and fig. S1D). Sanger sequencing of tumor cells derived from mice infected with Ad-gEp300/Cas9-Cre consistently identified insertion mutations (c.4411_4412insA/G) in exon 27 of *Ep300*, resulting in a premature STOP codon and ~161-kDa truncated EP300 variant (Fig. 2E). Consistently, immunoblot with antibodies against N terminus of EP300 demonstrated loss of full-length EP300 (closed arrowhead) and expression of the truncated variant (open arrowhead) in primary tumor cells from mice infected with Ad-gEp300/Cas9-Cre (Fig. 2F). These findings suggested that CRISPR-mediated targeting of the HAT domain decreases the expression of full-length EP300 while inducing the expression of EP300 variants lacking most of the HAT domain and others domains at the C terminus. Given that loss of *Ep300* abolished tumor development, while elimination of the HAT domain could drive tumor development, we surmised that the protumorigenic role for EP300 in SCLC is due to the activity of N-terminal domains, including TAZ, KIX, and BRD.

EP300 KIX is required for SCLC growth

We next sought to determine the contribution of the TAZ1, KIX, and BRD domains to tumor development using a precancerous neuroendocrine cell (preSC)–based model of SCLC development (*22*). Similar to mouse models, CRISPR-mediated targeting of *Ep300* exon 27 in *Rb1*- and *Trp53*-deficient precancerous neuroendocrine resulted in loss of full-length EP300 and expression of

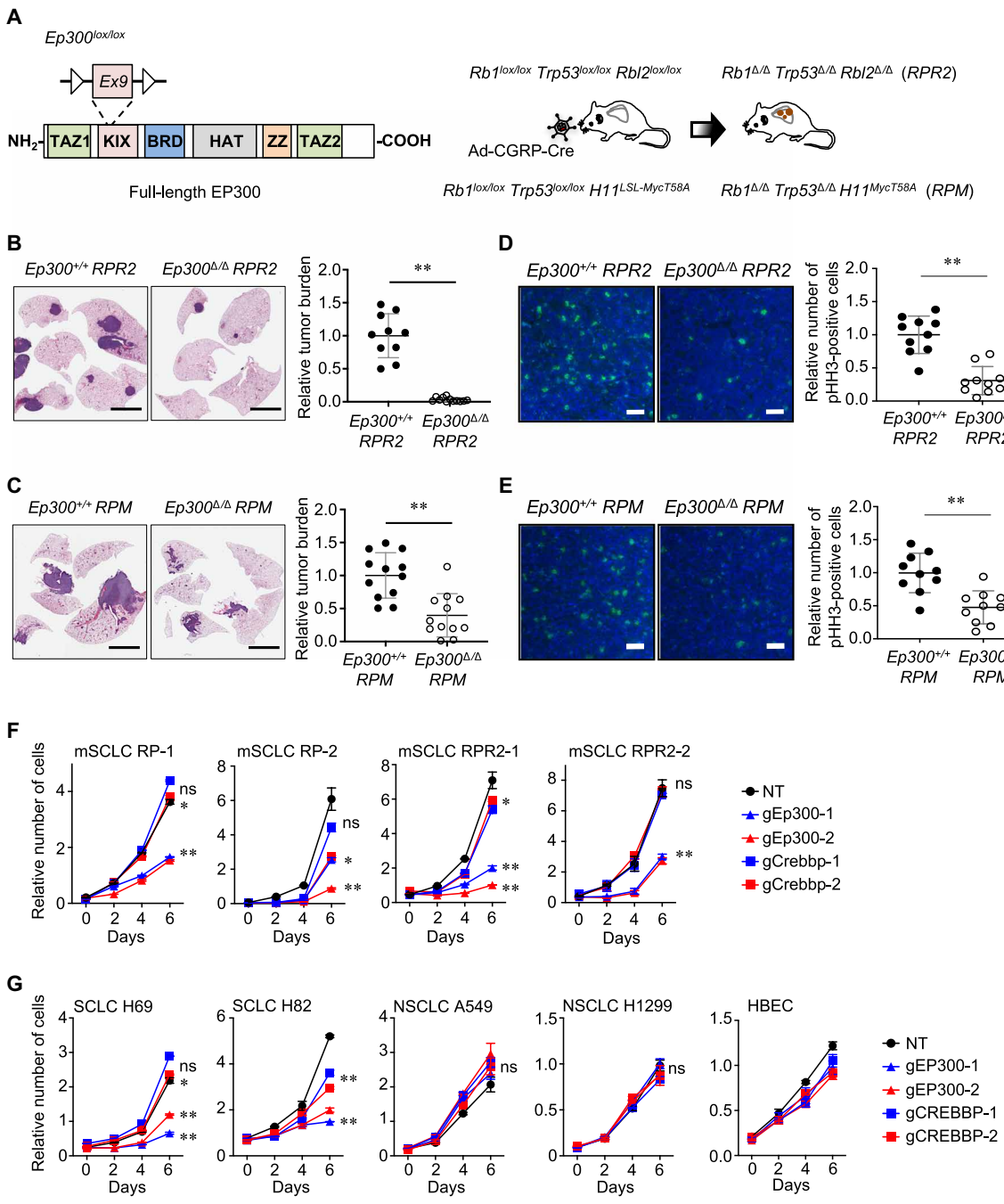

Fig. 1. Tumor-suppressive effect of *Ep300* KO on tumor development. (**A**) Diagrams of the floxed *Ep300* allele and EP300 domains (left) and schematics of Cre-driven lung tumor development in *RPR2* and *RPM* mice (right). (**B** and **C**) Representative images of hemotoxylin and eosin (H&E)–stained lung sections and quantification of tumor burden (tumor area/lung area) in $Ep300^{+/+}$ versus $Ep300^{\Delta/\Delta}$ *RPR2* ($n = 10$ and 12, respectively) (B) and $Ep300^{+/+}$ versus $Ep300^{\Delta/\Delta}$ *RPM* mice ($n = 12$ tumors per genotype) (C) (right). (**D** and **E**) Representative images of immunostained lung sections and quantification of pHH3-positive cells per lung area in $Ep300^{+/+}$ versus $Ep300^{\Delta/\Delta}$ *RPR2* (D) and $Ep300^{+/+}$ versus $Ep300^{\Delta/\Delta}$ *RPM* ($n = 10$ tumors per genotype) (E). (**F** and **G**) Results of CellTiter-Glo assays for mouse SCLC cells (RP-1 and RPR2-1), derived from the tumors developed in *RP* (*Rb1/Trp53*-mutant) and *RPR2* mice (F), and human SCLC and NSCLC lines expressing CRISPR-Cas9 and gRNAs against *Ep300/EP300* or *Crebbp/CREBBP* or a nontargeting gRNA (NT). *$P < 0.05$ and **$P < 0.01$. Statistical tests performed using unpaired *t* test (ns, not significant). Error bars represent SD. Scale bars, (B and C) 5 mm and (D and E) 50 μm. HBEC, human bronchial epithelial cell.

EP300 variants lacking the HAT domain and the rest of C terminus (Fig. 3A and fig. S3, A and B). These mutant cells, designated $Ep300^{\Delta HAT}$preSCs, transformed into spheroids and showed higher colony-forming capacity than control preSCs in soft agar culture (Fig. 3B). Consistent with the tumor-promoting impact of targeting *Ep300* exon 27, these findings demonstrate the tumor suppressor of the HAT domain. We then performed CRISPR-mediated targeting of the exons encoding TAZ, KIX, and BRD domains. Targeted

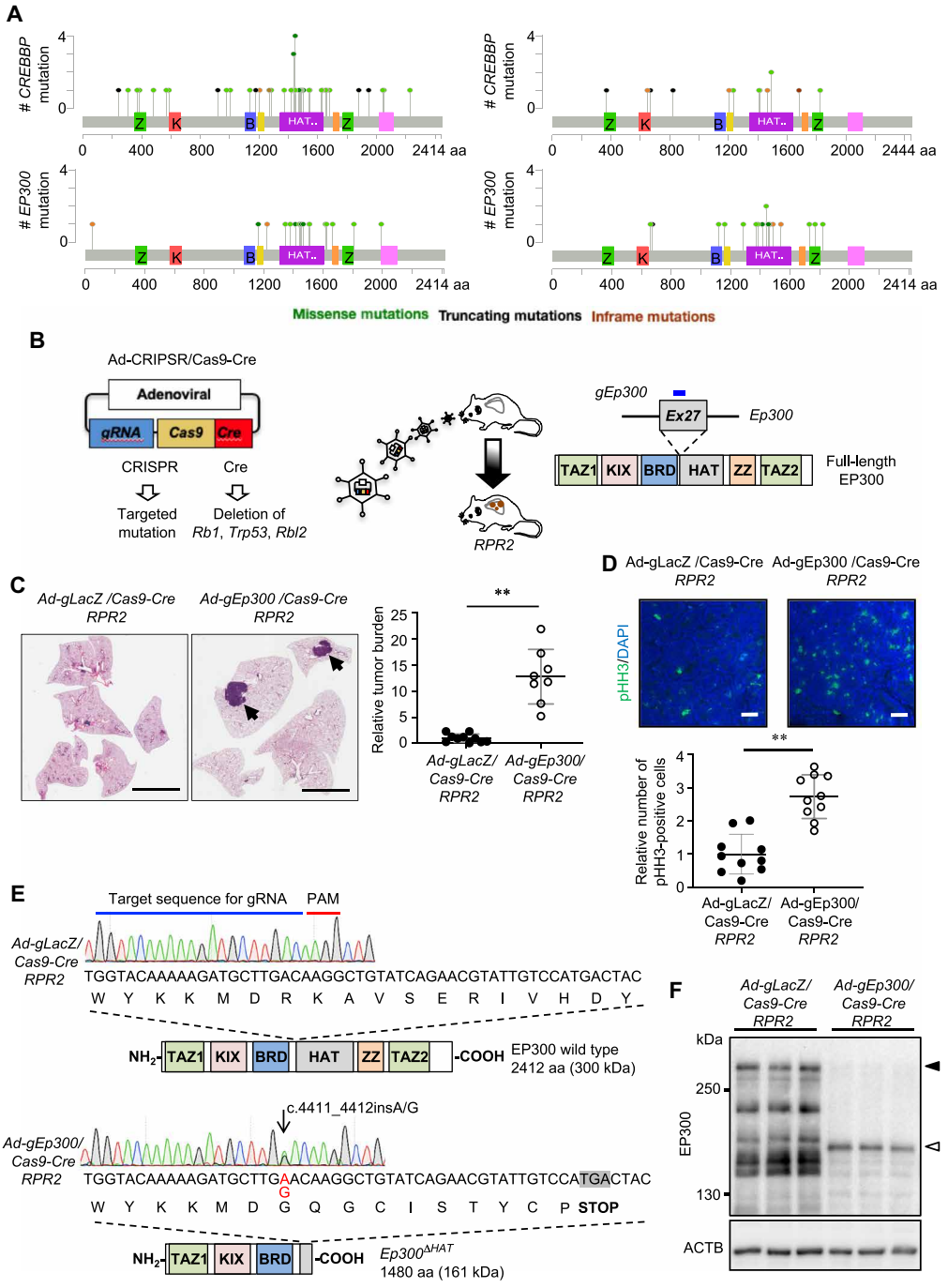

Fig. 2. Tumor-promoting effect of inactivating EP300 HAT domain on tumor development. (**A**) The patterns of *EP300* and *CREBBP* mutations in human tumors. Lollipop diagrams generated from cBioportal show the distribution of mutations in the genes with respect to the protein structures. In both the published data from George *et al.* (*5*) and Rudin *et al.* (*7*) (left) and the data from the MSK-IMPACT clinical sequencing cohort (right), mutations that would result in loss of function are lacking in the coding sequences for the EP300 KIX domain but occur in the coding sequences for CREBBP KIX domain. Z, TAZ domain; K, KIX domain; B, bromodomain; HAT, HAT domain. (**B**) Schematics of adenoviral CRISPR-Cre hybrid vector and targeting of *Ep300* exon 27 in the lungs of *RPR2* mice. (**C**) Representative images of H&E-stained lung sections of *RPR2* mice infected with Ad-gLacZ/Cas9-Cre versus Ad-gEp300/Cas9-Cre virus expressing Cre and gRNAs against *LacZ* (gLacZ) and *Ep300* (gEp300) (left) and quantification of tumor burden (tumor area/lung area, $n = 10$ and 8, respectively) (right). Arrowheads indicate nodular lung tumors. (**D**) Representative images of immunostained lung sections of $Ep300^{+/+}$ versus $Ep300^{\Delta/\Delta}$ *RPR2* mice and quantification of pHH3-positive cells per lung area in Ad-gLacZ/Cas9-Cre versus Ad-gEp300/Cas9-Cre infected mice ($n = 10$ tumors per genotype). (**E**) Chromatograms showing results of Sanger sequencing of the region the gRNA target sequences (chromosome 15: 81,525,569 to 81,525,602) in mice infected with Ad-gLacZ/Cas9-Cre or Ad-gEp300/Cas9-Cre. Arrow indicates the insertion mutation. Sequences are aligned with the diagram of wild-type and mutant EP300 proteins. c.4411_4412insA/G mutations (in red) caused by Ad-gEp300/Cas9-Cre result in a premature stop codon. (**F**) Immunoblot for EP300 in primary cells derived from the lung tumors. Closed and open arrowheads indicate wild-type and variant EP300, respectively. ACTB (beta-actin) blot for a protein loading control. $^{**}P < 0.01$. Statistical tests performed using unpaired *t* test. Error bars represent SD. Scale bars, (C) 5 mm and (D) 50 μm. aa, amino acid.

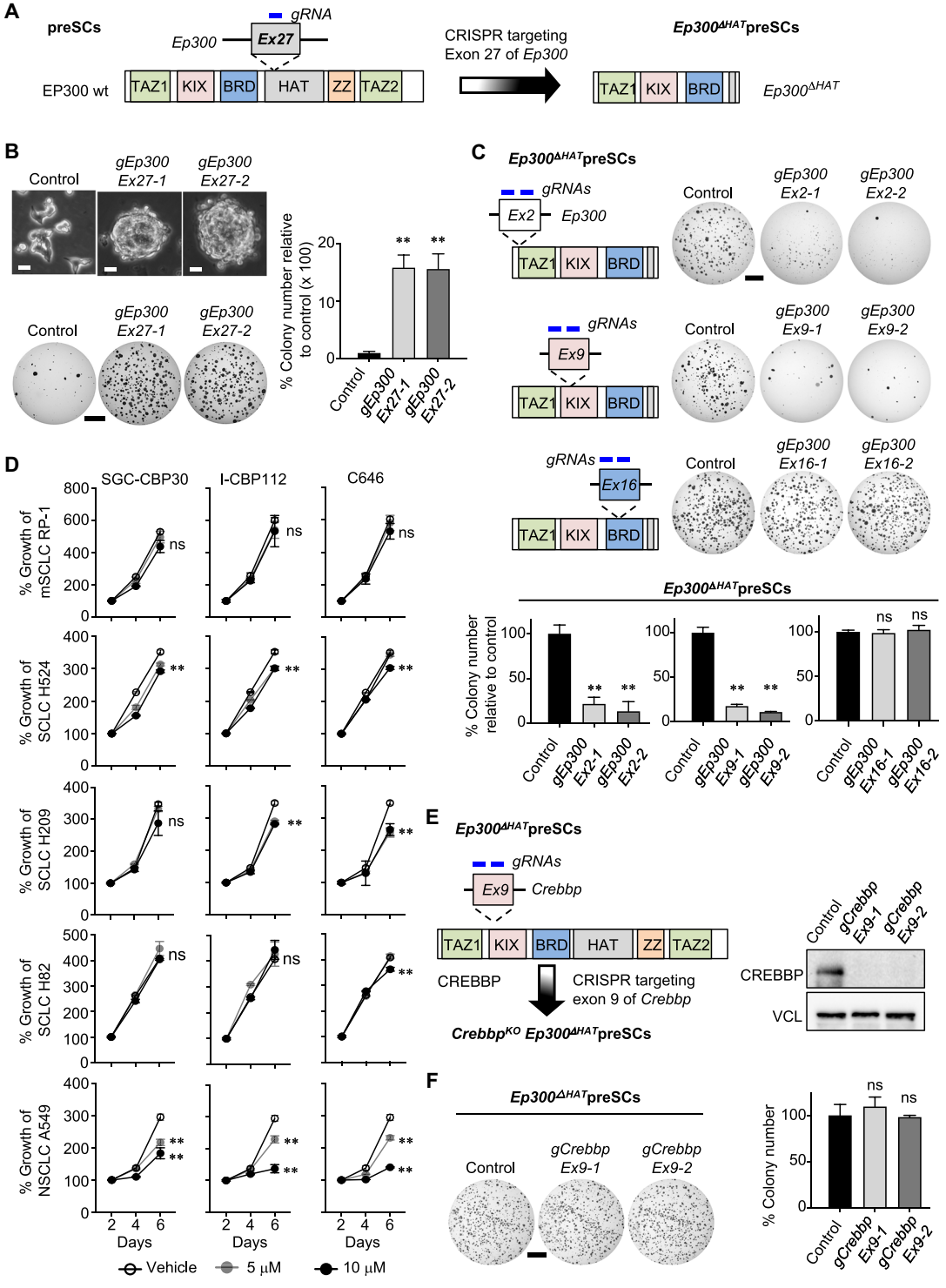

Fig. 3. Role of EP300 KIX domain in SCLC cell proliferation. (**A**) Schematics of generating *Ep300*$^{\Delta HAT}$preSCs by CRISPR targeting of *Ep300* exon 27, resulting in an EP300 variant lacking HAT and additional C-terminal domains. wt, wild type. (**B**) Representative images of control preSCs and *Ep300*$^{\Delta HAT}$preSCs in culture and soft agar (left) and quantification of colonies >0.2 mm in diameter (right) ($n = 3$ per cell type). (**C**) Schematics of CRISPR-mediated targeting of exons 2, 9, and 16 in *Ep300*$^{\Delta HAT}$preSCs (left) and representative images and quantification of colonies in soft agar ($n = 3$ per cell type) (right). (**D**) Results of MTT cell viability assay of mouse SCLC cells (RP-1) and human SCLC and NSCLC cell lines treated with selective bromodomain (BRD) inhibitors of CREBBP/EP300 (I-CBP112 and SGC-CBP30) and a selective HAT domain inhibitor of CREBBP and EP300 (C646) ($n = 3$ per cell type). (**E**) Schematics of generating *Crebbp*^{KO}*Ep300*$^{\Delta HAT}$preSCs (left) and immunoblot for CREBBP in CRISPR-targeted *Ep300*$^{\Delta HAT}$preSCs (right). VCL (Vinculin) was used as a protein loading control. (**F**) Representative images and quantification of soft agar colonies formed from *Crebbp* targeted and control *Ep300*$^{\Delta HAT}$ cells (right) ($n = 3$ per cell type). $^{**}P < 0.01$. Statistical tests performed using unpaired *t* test. Error bars represent SD. Scale bars, (B) 10 μm (top) and 5 mm (bottom) and (C and F) 5 mm.

mutations in exon 2, which result in deletion of all three domains, markedly reduced the ability of $Ep300^{\Delta HAT}$preSCs to form colonies in soft agar compared with nontargeted control cells (Fig. 3C and fig. S3, C and D). A similar decrease in soft agar growth was seen with targeting of exon 9, expected to result in loss of function of the KIX and BRD (Fig. 3C and fig. S3, C and D). However, targeting of exon 16, which disrupts the function of the BRD domain in $Ep300^{\Delta HAT}$preSCs, did not have any significant effect on the cell growth in soft agar (Fig. 3C and fig. S3, C and D). Alternatively, we inhibited the BRD and HAT domains in CREBBP and EP300 using selective small-molecule inhibitors SGC-CBP30 and I-CBP112 (for BRD) and C646 (for HAT) (*23*–*25*). The inhibitors did not have any significant effect on the growth of mouse SCLC cell line (RP-1) in culture, and their effects on human SCLC cell lines were either insignificant or modest (Fig. 3D). In contrast, the inhibitors had dose-dependent effects on NSCLC lines (Fig. 3D), as recently reported (*26*). Together, these findings suggest that the KIX domain is not only necessary and sufficient for the oncogenic function of EP300 in SCLC but also raised the question about any role for the homologous CREBBP KIX domain upon the loss of EP300 KIX. However, when we knocked out CREBBP in $Ep300^{\Delta HAT}$preSCs, we did not observe any significant impact on the cell growth in soft agar (Fig. 3, E and F), further highlighting the distinct role for the EP300 KIX in cell growth.

We postulated that the growth inhibitory effect of deleting the EP300 KIX domain is attributed to resulting loss of its interaction with TFs critical for cell proliferation and survival (Fig. 4A) (*27*). To test this idea, we individually knocked out the genes encoding known KIX-interacting factors using CRISPR-Cas9 method (Fig. 4, B and C). KO of CREB1 (cAMP response element binding protein 1), MYB (v-myb myeloblstosis viral oncogene homolog), JUN (v-jun sarcoma virua 17 homolog), ATF1 (activating transcription factor 1), and ATF4 inhibited the growth of $Ep300^{\Delta HAT}$preSCs in soft agar, whereas KO of SREBF2, (sterol regulatory element binding transcription factor 2), RELA (v-rel reticuloendotheliosis viral oncogene homolog a), GLI3 (glioma-associated oncogene family zinc finger 3), and KMT2A (lysine methyltransferase 2A) did not (Fig. 4B). Because these factors also bind to the CREBBP KIX domain (*27*), we tested whether the growth inhibition was, in part, due to disruption of the CREBBP KIX-protein interactions. Targeting the same factors in $Crebbp^{KO}Ep300^{\Delta HAT}$preSCs resulted in a growth inhibition nearly identical to that in $Ep300^{\Delta HAT}$preSCs (Fig. 4C), suggesting, again, a specific role for the EP300 KIX. Furthermore, because the growth inhibitory effects of reducing CREB1, ATF4, MYB, or JUN may be independent of their interaction with the KIX domain of EP300, we determined what extent knocking out the KIX-interacting TFs affect the cell growth in the absence of EP300 KIX domain. Using $Ep300^{Ex2}$preSCs completely lacking EP300 (Fig. 3C), we targeted the TFs individually using CRISPR-Cas9. While these EP300 KO cells did not grow well as expected (Fig. 3C), a short-term growth assay showed that the KO of CREB1, ATF4, or JUN resulted in a modest but significant reduction of cell growth, whereas the KO of MYB had no significant effect on cell growth (fig. S4). These results suggest that CREB1, ATF4, and JUN promote cell growth partially via EP300-indepdent pathways, in addition to their interactions with EP300, while MYB depends more on the interaction with EP300. Together, these findings reveal a previously unidentified mechanism underlying SCLC development, which is dependent on and unique to the EP300 KIX domain.

An alanine-versus-aspartate difference in the EP300 and CREBBP KIX domains defines differential binding affinities of the proteins to KIX-binding partners

TFs involved in proliferation and survival are known to bind to the KIX domain via common binding sites known as MLL (mixed lineage leukemia) and MYB sites (Figs. 4A and 5A) (*27*). We thus sought to determine whether we could target these interactions to inhibit SCLC development and growth. We used a fluorescence polarization (FP) assay (*28*) to measure the binding affinity of the KIX-mediated interactions using the purified KIX domains of EP300 and CREBBP and fluorophore-labeled KIX-binding sequences of MLL (MLL25) and MYB (MYB25). Purified EP300 KIX bound to MLL25 and MYB25 with higher affinity [dissociation constant (K_d) = 40 ± 14 μM and 3.8 ± 0.2 μM, respectively] than CREBBP KIX (K_d = 94 ± 11 μM and 22 ± 4.1 μM, respectively) (Fig. 5B). The differential affinities of the EP300 and CREBBP KIX domains for MLL and MYB have not been previously known but may result from several differences in the amino acid sequences, including Asp^{647} in CREBBP KIX domain which is Ala^{627} in the EP300 KIX domain (Fig. 5A). In contrast to Asp^{647} (D647) in the CREBBP KIX domain, Ala^{627} (A627) in the EP300 KIX domain may mediate a hydrophobic interaction with Met^{303} of MYB25 that results in higher binding affinity between the EP300 KIX domain and interacting partners (Fig. 5A). To test this, we substituted Asp^{647} in the CREBBP KIX domain with alanine (D647A) to mimic A627 in EP300 KIX domain. This single–amino acid change resulted in a K_d of 6.7 ± 0.5 μM for binding of the D647A CREBBP KIX domain to MYB (Fig. 5C), a threefold increase in binding affinity and quite similar to the 3.8 μM value we observed for the EP300 KIX domain (Fig. 5B). In reverse, substitution of Ala^{627} in the EP300 KIX domain with aspartate (A627D), which mimics Asp^{647} in CREBBP KIX domain, resulted in K_d values of 23 ± 6.2 μM and 80 ± 8.5 μM for binding to MYB and MLL peptides, respectively (Fig. 5C). These K_d values for the A627D EP300 KIX were found to be very similar to the wild-type CREBBP KIX domain (Fig. 5B).

Next, to test whether we could disrupt the interactions between the KIX domain and MLL and MYB, we generated a fusion peptide MLL28MYB30 (M/M) consisting of 28 residues from the MLL activation domain and 30 residues from the MYB activation domain linked by two glycine residues (GG) (Fig. 5D). This design is based on data suggesting that MLL and MYB can bind cooperatively to the KIX domain to form a ternary complex that prevents other factors from binding to their respective sites in leukemia and other cell types (*29*) and that MYB and MLL could be tethered together via their interactions with Menin (*30*). As a control, we also made a variant of M/M (M/M-5A) with five alanine substitutions of critical residues important for the binding of MLL and MYB to the KIX domains. M/M inhibited binding of the fluorescein isothiocyanate (FITC)–labeled MYB and rhodamine-labeled MLL peptides to the EP300 KIX domain with a median inhibitory concentration (IC_{50}) value of 8.5 ± 0.7 μM and 8.3 ± 0.5 μM, respectively (Fig. 5E). M/M also inhibited the binding of MYB and MLL peptides to the CREBBP KIX domain but, at higher IC_{50} values, 22 ± 2.3 μM and 23 ± 1.3 μM, respectively. M/M-5A did not have any effect even at high concentrations (Fig. 5E). Immunoprecipitation followed by immunoblot confirmed the binding of M/M to both EP300 and CREBBP and indicated that, consistent with the results of the in vitro binding assay (Fig. 5B), M/M bound preferentially to EP300 than to CREBBP (Fig. 5F). We measured the K_d values for binding of the M/M and

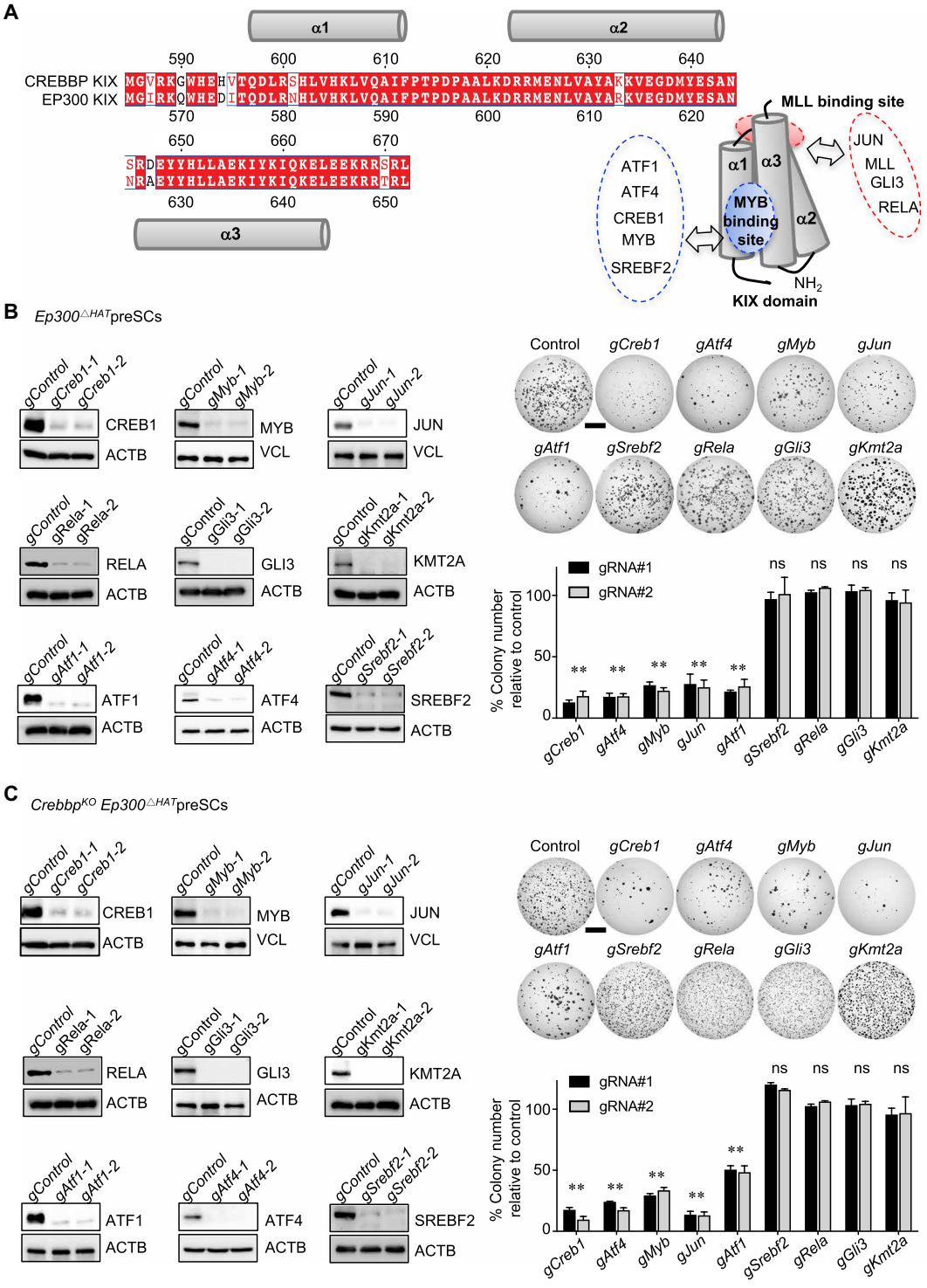

Fig. 4. Effects of knocking out TFs known to interact with EP300/CREBBP KIX domains. (**A**) Alignment of the amino acid sequences of human CREBBP and EP300 KIX domains. Numbering of residues is based on the CREBBP KIX domain (left). Cylinder representation of the structure of the KIX domain with MLL and MYB binding sites (right). Included in the dotted lines are the TFs known to bind to the MLL/MYB sites. (**B** and **C**) Immunoblots validate loss of EP300/CREBBP KIX domain–interacting partner proteins (left) and representative images and quantification of soft agar colonies formed from targeted $Ep300^{\Delta HAT}$preSCs or $Crebbp^{KO}Ep300^{\Delta HAT}$preSCs as indicated ($n = 3$ per cell type) (right). ACTB and VCL blots were used as protein loading controls. $^{**}P < 0.01$. Statistical tests performed using unpaired *t* test. Error bars represent SD. Scale bars, (B and C) 5 mm.

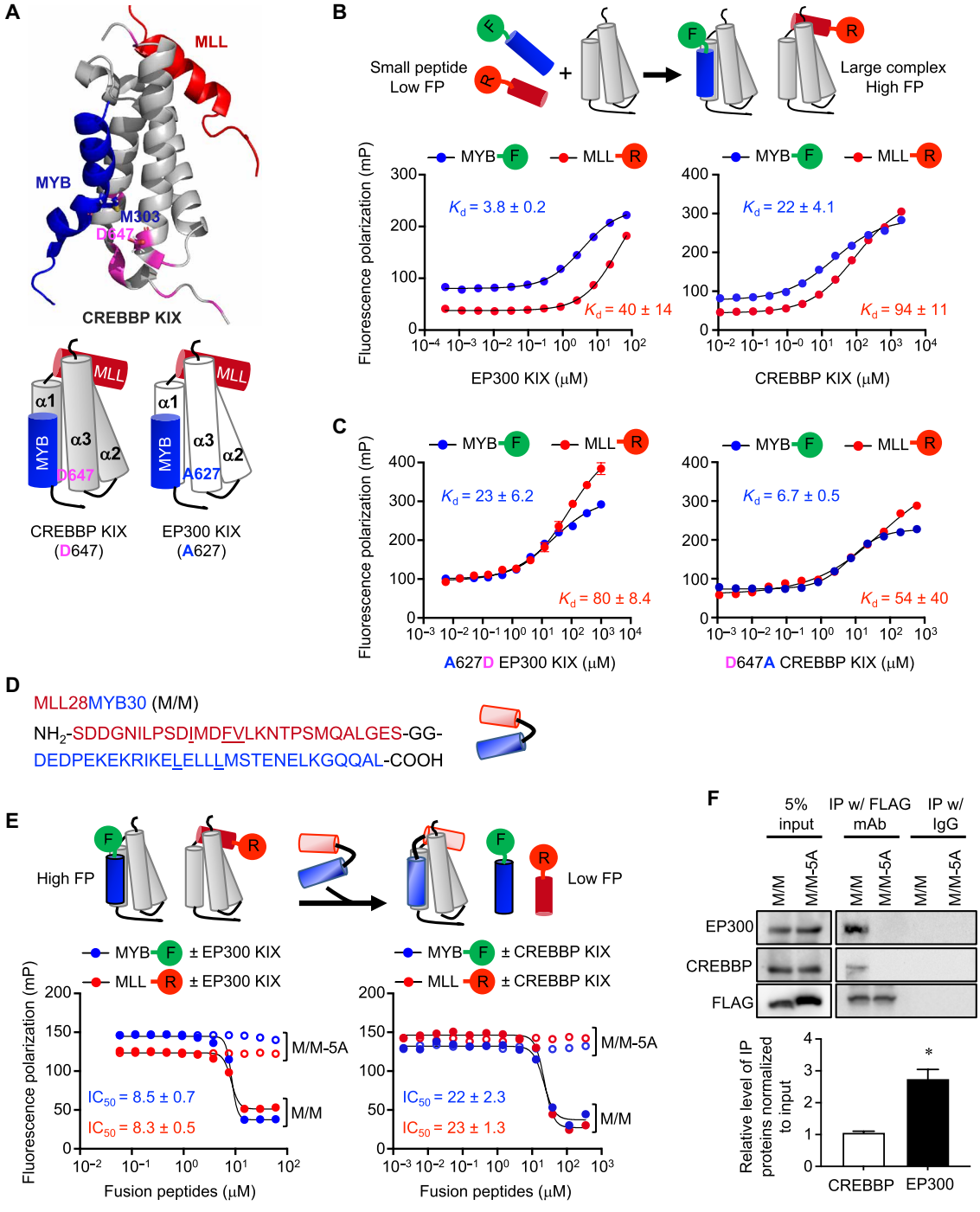

Fig. 5. Differential binding affinities of EP300 and CREBBP KIX domains with MLL and MYB. (**A**) The structure of CREBBP KIX domain interacting with the MLL25 and MYB25 peptides representing 25–amino acid fragments of MLL and MYB, respectively (Protein Data Bank ID: 2AGH) (top). Residues highlighted in magenta represent key differences between the CREBBP and EP300 KIX domains, including Asp^{647}. Cylinder diagrams of the interactions between the CREBBP/EP300 KIX domain and MLL25 and MYB25 (bottom). The positions of Asp^{647} and Ala^{627} in CREBBP and EP300, respectively, are indicated. (**B**) Schematic of the FP assay to examine binding with rhodamine (R)–tagged MLL25 and FITC (F)–tagged MYB25 by the purified KIX domains of CREBBP and EP300 (top). K_d values indicate the binding affinities of the purified KIX domains for the fluorophore-labeled peptides (bottom). (**C**) Results of the FP assay to examine binding with fluorophore-labeled MLL25 and MYB25 by A627D EP300 KIX (left) and D647A CREBBP KIX (right). (**D**) Amino acid sequence of the fusion peptide MLL28MYB30 (M/M) with a GG linker (left) and diagram of M/M peptide with the linker (right). The underlined amino acids were replaced with alanine in the mutant variant M/M-5A. (**E**) Schematic showing displacement of fluorophore-labeled peptides by M/M (top). Inhibition curves (bottom) showing the impact of M/M and M/M-5A on binding of the EP300 and CREBBP KIX domains to fluorophore-labeled peptides. (**F**) Immunoblots for FLAG, EP300, and CREBBP in H524 cell extracts after immunoprecipitation (IP) with anti-FLAG antibodies or isotype immunoglobulin G. The cell extracts (5%) were used to show protein levels in input (top). Quantification of intensity of the bands following IP, relative to input band ($n = 3$) (bottom). *$P < 0.05$. Statistical tests performed using unpaired *t* test. Error bars represent SD. mAb, monoclonal antibody.

M/M-5A peptides to the KIX domains of EP300 and CREBBP using isothermal titration calorimetry (ITC) (fig. S5), yielding K_d values of 30 and 44 nM for binding of M/M to the EP300 KIX domain and CREBBP KIX domain, respectively. No binding was observed for the M/M-5A peptide. These values are in good agreement with a recent report for a similar peptide fusion of MYB and MLL, which reported K_d values in the low nanomolar range for the CREBBP/EP300 KIX domain (*31*).

KIX domain is vulnerable to peptide inhibition

Given that M/M appears to specifically inhibit EP300 KIX-mediated protein interactions, we asked whether it results in the same tumor-suppressive impact of inactivating the KIX domain. We expressed M/M in SCLC lines using a doxycycline-inducible lentivirus vector to determine the functional impact of disrupting these interactions (Fig. 6A). M/M inhibited the short-term proliferation and the ability of SCLC cells to form colonies in soft agar, whereas M/M-5A did not have any significant effects (Fig. 6, B and C). Notably, both M/M and M/M-5A did not detectably affect the growth of lung adenocarcinoma cell lines (Fig. 6, B and C). To test whether levels of the KIX-interacting partners determine this differential sensitivity to M/M, we examined the proteins whose KO inhibits cell growth (Fig. 4B). Immunoblots showed that compared to SCLC cells, lung adenocarcinoma cell lines expressed lower levels of KIX domain–interacting proteins (Fig. 6D). These results not only support the importance of the EP300 KIX domain for the growth of SCLC cells but also suggest selective binding of the EP300 KIX domain to key interaction partners involved in proliferation and survival.

To gain insight into the cellular processes that are altered by this blockade, we performed RNA sequencing and analyzed transcriptomic changes in H209 and H524 SCLC cell lines expressing M/M or M/M-5A. The heatmap plots show the distinct sets of genes clustered into M/M and M/M-5A groups in both H524 and H209 cell lines (fig. S6, A and C). To assess the impact of disrupting the interaction between KIX domain and its interacting TFs on each TF-related gene expression and targets, we performed gene set enrichment analysis (GSEA). Using the differentially expressed genes (DEGs) between the M/M and M/M-5A cells (table S2), we queried the gene set signatures in the Molecular Signatures Database v7.4. The GSEA results showed that the genes affected by KIX domain blockade (M/M) in H524 and H209 were significantly enriched in the gene sets related to MYB, ATF4, CREB1, and CREBP1/JUN targets with a large number of leading edge genes (fig. S6, B and D, and table S3). In addition, to gain insight into the cellular processes that are affected by EP300 KIX-protein interactions, we performed Kyoto Encyclopedia of Genes and Genomes analysis of the DEGs (fig. S7). The top 10 most significant pathways down-regulated by the M/M-driven perturbation of the KIX-TF interaction included the proliferation-related pathways, including "cell cycle," "purine/pyrimidine metabolism," and "dna replication." Notably, the pathway "small cell lung cancer" was also down-regulated in M/M-expressing H209 cells. Together, these results are in line with the inhibitory effects of M/M on the EP300 KIX domain–TF interaction and SCLC growth.

The results from our proof-of-concept experiments above encouraged us to explore the feasibility of using small molecules to block KIX domain–protein interactions and regulate cell growth. KG-501 (2-naphthol-AS-E-phosphate) and its derivative 666-15 have been shown to inhibit the interaction between CREB1 and the KIX domains of EP300 and CREBBP (*32*, *33*). KG-501 inhibited the short-term growth of SCLC lines in culture and colony formation in soft agar but did not have a significant effect on NSCLC cell lines (Fig. 7A and fig. S8A). Likewise, 666-15 inhibited the growth of SCLC lines but did not affect the growth of NSCLC cell lines (Fig. 7, B and C, and fig. S8B). Given its improved potency and bioavailability compared with KG-501 (*33*, *34*), 666-15 was tested for its potential effect on tumor growth in vivo. Daily intraperitoneal treatment with 666-15 suppressed the formation of subcutaneous tumors derived from mouse SCLC cells in immune-competent mice (129S/B6 F1 hybrid), without significant weight loss (Fig. 7D and fig. S8C). Encouraged by this result, we then tested the effects on SCLC development of treating *RPR2* mice with daily 666-15, beginning 180 days after tumor induction (Fig. 7E). A conditional luciferase allele *Rosa26*$^{\text{lox-stop-lox-Luc}}$ carried by these mice allowed for bioluminescence imaging to monitor the tumorigenic growth of mutant cells. After 4 weeks of treatment, bioluminescence measurement indicated a lower tumor burden in the inhibitor-treated mice than the vehicle-treated controls (Fig. 7F). Furthermore, a moderate but significant improvement in survival outcomes was observed in mice treated with 666-15 compared with the vehicle (Fig. 7G). These results provide further evidence for the importance of the KIX domain for the growth of SCLC cells and strongly support for the feasibility of targeting KIX-mediated interactions for the treatment of SCLC in vivo.

DISCUSSION

We report that EP300 plays both protumorigenic and tumor-suppressive roles driven by the functions of KIX and HAT domains, respectively. This dual role of EP300 in SCLC is remarkable in that, despite the high structural and functional similarity, CREBBP only plays a tumor-suppressive role through its HAT domain while its KIX domain is dispensable. Notably, these differential requirements for the KIX domain of EP300 and CREBBP in SCLC are in line with the SCLC genome in which detrimental mutations are lacking in the coding sequences in *EP300* for the N terminus and KIX domain while these mutations occur along the entire length of coding sequence in *CREBBP* (Fig. 2). This EP300 mutation pattern may be unique to SCLC as the mutation patterns in *EP300* and *CREBBP* are similar in lymphoma and other cancer types in which functional loss of either EP300 or CREBBP is thought to promote tumorigenesis (*10*). The necessity of the EP300 KIX domain also appears unique to SCLC as *Ep300* KO did not affect development of *Kras*$^{\text{G12D}}$-driven lung adenocarcinoma in mice (fig. S2E) and inhibition of both EP300 and CREBBP KIX domains did not affect proliferation of lung adenocarcinoma cells (Figs. 6 and 7). Recent studies demonstrated that the combined loss of EP300 and CREBBP, specifically the loss of BRD and HAT domain activities, suppressed the proliferation of *Kras*-mutant lung adenocarcinoma, lymphoma, and leukemia cell lines (*25*, *26*, *35*, *36*). In contrast, numerous solid tumors—including melanoma, triple-negative breast cancer, and SCLC lines—were much less sensitive to a potent inhibitors of HAT activity (*25*). Similarly, our results suggest that the BRD and HAT domains have little or no significant effect on promoting cell growth.

Our results suggest that the unique dependency on EP300 KIX domain is due, in part, to the higher affinity (~6-fold) of the EP300 KIX for protumorigenic TFs such as MYB compared with the CREBBP KIX domain. This raises a fundamental question about

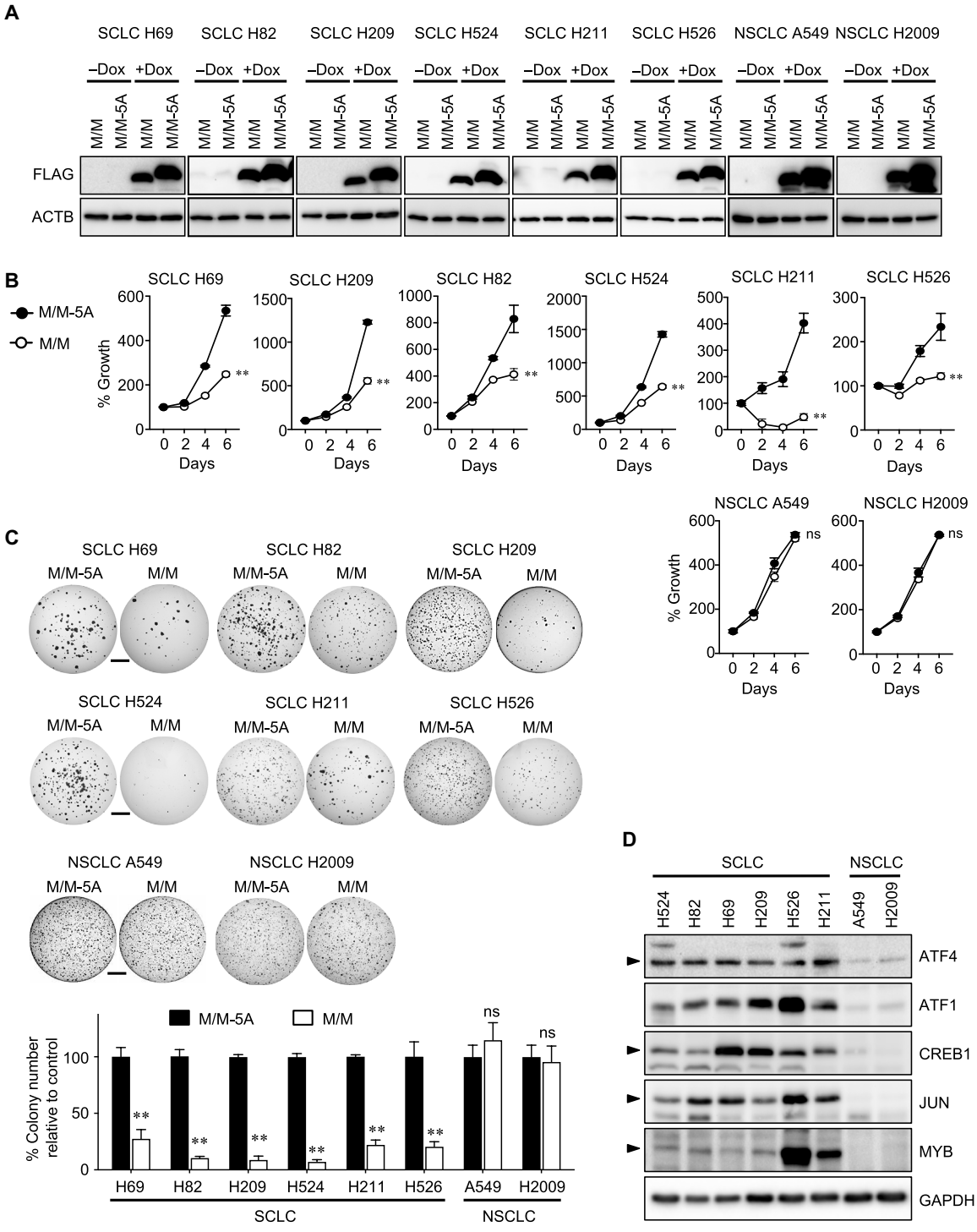

Fig. 6. Effects of disrupting KIX domain–mediated protein interaction on cell proliferation. (**A**) Immunoblots for FLAG in SCLC and NSCLC lines expressing FLAG-tagged M/M or M/M-5A under the control of doxycycline (Dox)–inducible promoter. ACTB blot was used as protein loading control. (**B**) Results of MTT cell viability assay of human SCLC and NSCLC cell lines expressing M/M or M/M-5A ($n = 3$ per cell type). (**C**) Representative images and quantification of soft agar colonies (>0.2 mm) from human SCLC and NSCLC cell lines expressing M/M or M/M-5A ($n = 3$ per cell type). (**D**) Immunoblots for KIX domain–interacting proteins in SCLC and NSCLC lines. Glyceraldehyde-3-phosphate dehydrogenase (GAPDH) was used a loading control. Arrowheads indicate specific bands. Statistical tests performed using unpaired *t* test. Error bars indicate the SD in measurements. $^{**}P < 0.01$. Scale bars, (C) 5 mm.

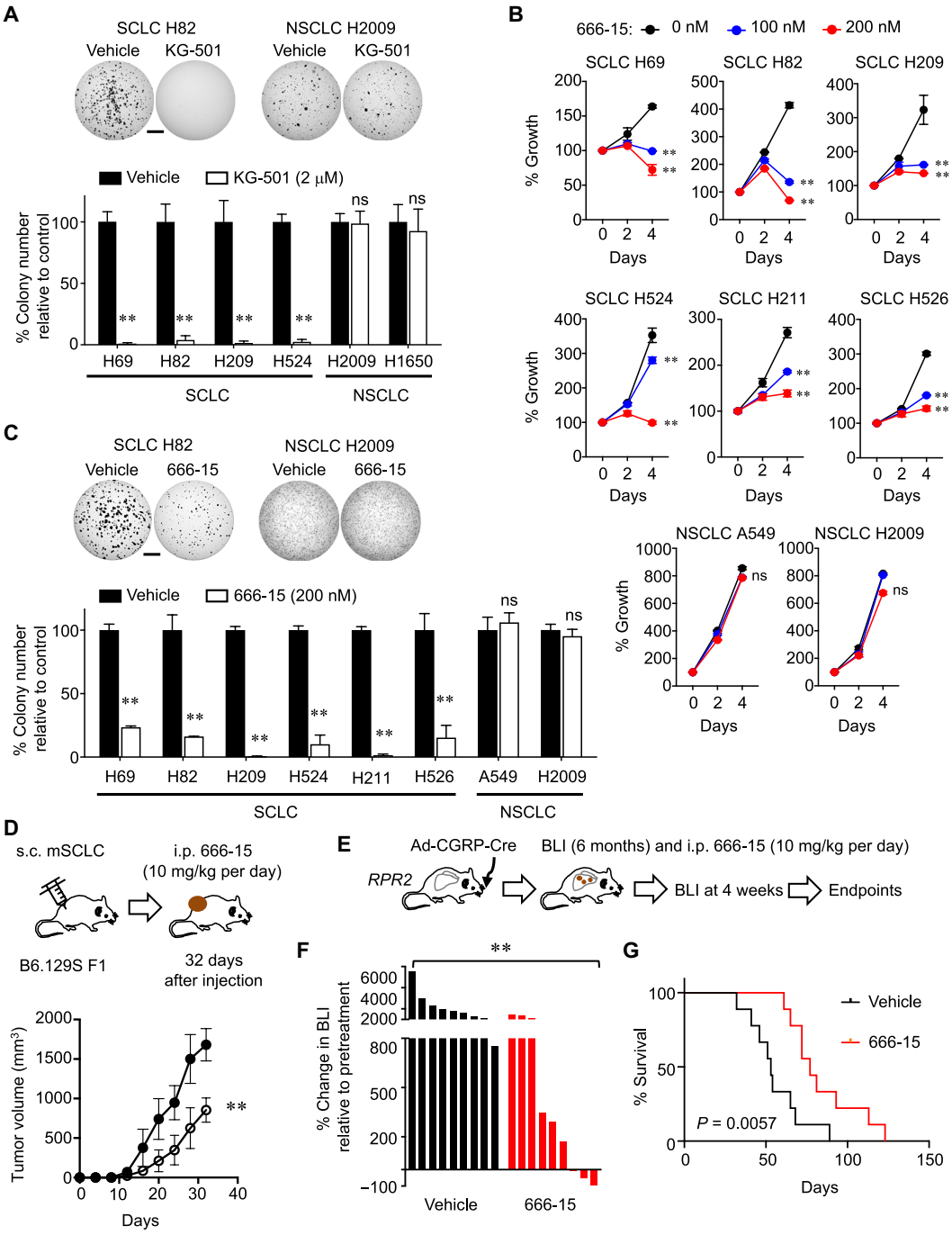

Fig. 7. Chemical inhibition of the KIX domain suppresses SCLC cells proliferation and tumor development. (**A**) Representative images and quantification of soft agar colonies (>0.2 mm in diameter) ($n = 3$ per cell type). Lung cancer cell lines were treated with 2 μM KG-501 in dimethyl sulfoxide (DMSO) or equal volume DMSO (control) throughout the assay. (**B**) Results of MTT cell viability assay of human SCLC and NSCLC cell lines treated with 100 and 200 nM concentrations of 666-15 or vehicle ($n = 3$ per cell type). (**C**) Representative images of soft agar colonies and quantification of colonies >0.2 mm in diameter ($n = 3$ per cell type). Lung cancer cell lines were treated with 200 nM 666-15 in DMSO or equal volume DMSO (control) throughout the assay. (**D**) Schematic describing generation of allograft tumors in B6.129S F1 hybrid mice followed by treatment with 666-15 or vehicle control (top) and plots of tumor volumes of allograft tumors formed in mice treated with vehicle or 666-15 ($n = 5$ tumors per group) (bottom). i.p., intraperitoneal; s.c., subcutaneous. (**E**) Schematic describing Cre-mediated induction of tumors in *RPR2* mice. (**F**) Quantification of changes in tumor volume per bioluminescence imaging (BLI), normalized to pretreatment BLI levels. The vehicle or drug treatment began 180 days after Ad-CGRP-Cre infection for tumor induction. BLI was performed after 4 weeks of treatment. Each bar represents an individual tumor. (**G**) Kaplan-Meier survival curves of *RPR2* mice treated with vehicle or 666-15 ($n = 9$ tumors per genotype). Log-rank (Mantel-Cox) test was used to determine the significance of tumor-free survival between the cohorts. $^{**}P < 0.01$. Statistical tests performed using unpaired *t* test. Error bar represents SD. Scale bars, (A and C) 5 mm.

what determines the affinities of these highly homologous KIX domains to their interacting partners. Swapping the aspartate residue in the CREBBP KIX domain and the alanine at the equivalent position in the EP300 KIX domain, we demonstrated that Ala^{627} in the EP300 KIX is important for the higher affinity to the interacting proteins. From these findings, we postulate that this alanine residue makes a hydrophobic interaction with Met^{303} in MYB, which results in higher binding affinity between the EP300 KIX domain and its interacting partners, while the aspartate in the CREBBP KIX does not. These results are significant in that they would provide insight into the molecular mechanism of functional differences between EP300 and CREBBP, which has long remained poorly understood. Although it is widely conceived that these proteins were functionally redundant and interchangeable (*1*, *37*, *38*), in vivo studies of genetically engineered mice suggested unique and shared functions of EP300 and CREBBP (*39*–*45*). In particular, the EP300 KIX domain, not the CREBBP KIX, is required for hematopoiesis in mice (*46*). The study then suggested the importance of the interaction between MYB and EP300. While it has been speculated the HAT-mediated activity was involved, it was not known how the specificity of the protein-protein interaction was achieved in vivo. Our in vitro binding assay using only the KIX domains suggest that the involvement of HAT domain is unlikely but point to the single–amino acid difference between EP300 and CREBBP as a determinant for their functional differences. Furthermore, our results also suggest that SCLC specificity of EP300 dependency is due, in part, to higher levels of the KIX domain–interacting factors in SCLC than NSCLC cells (Fig. 6). Therefore, we propose that the combination of this differential binding affinity and the availability of binding partners likely determines the effect strengths of the EP300 KIX domain on the downstream mechanisms, leading to tumorigenesis. This idea needs to be tested in future studies to predict the domain dependency in a given cell or in vivo.

The dependency of SCLC development on interactions mediated by the EP300 KIX domain represents a novel vulnerability in SCLC, a disease lacking in readily actionable oncogenic drivers. Thus, the tumor suppressive impact of inhibiting the protein interactions is significant. Besides the proof-of-concept experiment demonstrating the tumor-suppressive effect of a recombinant peptide blocker of the KIX-mediated protein interaction, the indication of a small-molecule inhibitor for the KIX domain may be readily translated to a novel therapeutic approach given the apparent low toxicity and the impact limited to SCLC.

MATERIALS AND METHODS

Mouse strains, tumor induction, and allografts

Strains of $Trp53^{lox}$, $Rb1^{lox}$, $Rbl2^{lox}$, $Ep300^{lox}$, $H11^{lox\text{-}stop\text{-}lox\text{-}MycT58A}$, and $Kras^{LSL\text{-}G12D}$ alleles were shared by A. Berns, T. Jacks, J. Sage, P. Brindle, T. Oliver, and R. Wechsler-Reya, respectively (*17*, *18*, *47*–*50*). Compound transgenic mice $Rb1^{lox/lox}$ $Trp53^{lox/lox}$ $Rbl2^{lox/lox}$ (*RPR*) mice and $Rb1^{lox/lox}$ $Trp53^{lox/lox}$ $H11^{lox\text{-}STOP\text{-}lox\text{-}MycT58A}$ (*RPM*) mice have been previously described (*18*, *20*). Mice were maintained according to the guidelines from the National Institutes of Health. Animal procedures were approved by the Institutional Animal Care and Use Committee (IACUC) at the University of Virginia. For tumor induction, lungs of 10-week-old mice were infected with adenoviral Cre via intratracheal instillation as previously described, and mice were aged 6 months (*51*). Multiple cohorts of independent litters were analyzed to control for background effects, and both male and female mice were used. Ad-CGRP-Cre particles were purchased from the University of Iowa Gene Transfer Vector Core. Ad-gLacZ/Cas9-Cre and Ad-gEp300/Cas9-Cre particles were produced in Vector Development Laboratory at Baylor College of Medicine. For allograft experiments, 5.0×10^5 murine cells were injected in the flanks of B6.129S F1 mice (the Jackson Laboratory). Perpendicular tumor diameters were measured using calipers. Volume was calculated using the formula $L \times W^2 \times 0.52$, where L is the longest dimension and W is the perpendicular dimension. The injected mice were maintained and observed for palpable tumors according to the procedures approved by the IACUC and euthanized when tumor size reached 1.5 cm in diameter, the endpoint of allograft study under the guideline of the institutional animal policy. The Kaplan-Meier curve was used to plot the time of survival (maximal tumor volume). For in vivo drug treatment experiments, *RPR* mice carrying $Rosa26^{LSL\text{-}Luciferase}$ were infected with Ad-CGRP-Cre and monitored by bioluminescence imaging to identify mice with tumor growth in the lungs. Mice anesthetized with isoflurane were injected with D-luciferin (150 mg/kg) (firefly) potassium salt (GOLDBIO, LUCK), and bioluminescence was detected using IVIS Spectrum (PerkinElmer) over 20 min to record the maximum radiance. The peak total flux values were assessed from the anatomical region of interest using Living Image 4.0 (PerkinElmer) and were used for analysis. 666-15 was dissolved in 1% *N*-methylpyrrolidone and 5% Tween 80 in H_2O. The mice were intraperitoneally injected with vehicle or 666-15 at 10 mg/kg once a day for the duration of experiments (*29*). Bioluminescence imaging was performed to follow tumor volume after treatment start, and weights were monitored weekly during the course of treatment.

Histology and immunohistochemistry

Mouse tissues were fixed in 4% paraformaldehyde in phosphate-buffered saline before paraffin embedding. Five-micrometer-thick tissue sections were stained with hematoxylin and eosin (H&E) staining and immunostaining. For quantification of pHH3-positive cells and CGRP staining, tumors of similar size and area were included. Macroscopic images of lung sections were acquired using Olympus MVX10. Images of H&E and immunostained tissues were acquired using Nikon Eclipse Ni-U microscope. Image analysis and automated quantification were performed using NIS-Elements Basic Research (Nikon).

Plasmids and chemicals

pCW57.1, pCW-Cas9, pL-CRISPR.EFS.tRFP, psPAX2, and pMD2.G plasmids were obtained from Addgene (nos. 41393, 50661, 57819, 12259, and 12260; the gifts from D. Root, E. Lander, D. Sabatino, B. Ebert, D. Trono, and P. Wright). LV-gRNA-zeocin plasmid was acquired from M. Adli (Northwestern University). To generate Ad-gLacZ/Cas9-Cre and Ad-gEp300/Cas9-Cre plasmids for adenovirus, we inserted in pENTR4 (an entry vector from Thermo Fisher Scientific), a DNA fragment consisting of U6 promoter, Cbh promoter, and sequences encoding CRISPR-Cas9-T2A-Cre recombinase in order. After inserting an oligonucleotide encoding gRNA at a Bbs I–cut site near the U6 promoter, we transferred all of the inserts from the entry vector to pAd/PL-DEST plasmid using Gateway cloning kits (Thermo Fisher Scientific). DNA fragment encoding P300 KIX in pUC57 was purchased from GenScript and cloned in pMAL c5e vector (New England Biolabs, N8110). A DNA fragment encoding

CBP KIX in pET-KIX was obtained from Addgene (plasmid no. 99336) and cloned in pMAL c5e vector. DNA fragments corresponding to the coding region of M/M and M/M-5A peptides were purchased from Integrated DNA Technologies and cloned in pENTR4 and subsequently in pCW57.1 using Gateway cloning kits (Thermo Fisher Scientific). pMAL-c5E (New England Biolabs, N8110) was used to express recombinant peptides for human EP300 KIX domain and CREBBP KIX domain. pET-32C vector was used to express M/M (wild-type and mutant) fusion peptides (28 residues from MLL activation domain and 30 residues from MYB activation domain linked by a GG linker). D647A mutant for CREBBP KIX and A627D mutant for EP300 KIX were generated using a site-directed mutagenesis kit (QuickChange XL from Agilent). Sequences of oligonucleotides for cloning and gRNAs are listed in the Supplementary Materials (table S1). All sequences were verified by Sanger sequencing. BRD inhibitors (SGC-CBP30 and I-CBP112) and HAT inhibitor (C646) were purchased from Sigma-Aldrich (SML1133, SML1134, and 382113, respectively). Inhibitors of CREB1-EP300/CREBBP KIX domains, KG-501 and 666-15, were purchased from Sigma-Aldrich (70485 and 538341, respectively).

Cell culture, lentiviral infection, and transient transfection

Murine SCLC cells and precancerous cells (preSCs) were derived from lung tumors and early-stage neuroendocrine lesions, respectively, developed in the *Rb1/Trp53*-GEMM (*20*, *22*). Human cell lines—including H69, H82, H209, H524, A549, H526, H211, H2009, and H1650—were the gifts from A. Gazdar and J. Minna (UT Southwestern), J. Sage (Stanford), H. Harada (Virginia Commonwealth University), and C. Vakoc (Cold Spring Harbor). These cell lines were authenticated by profiling patterns of 17 short tandem repeats (American Type Culture Collection, 135-XV and 200FTA) and tested negative for *Mycoplasma* using the PlasmoTest Mycoplasma Detection Kit (InvivoGen, rep-pt1). Experiments were performed within the first few passages after thawing frozen cell stocks. Cells were cultured in RPMI1640 medium (Cellgro) supplemented with 10% bovine growth serum (GE Healthcare, SH30541.03) and 1% penicillin-streptomycin (Invitrogen, 15140-122). Puromycin (Thermo Fisher Scientific, A11138-03) or zeocin (Thermo Fisher Scientific, R25001) was used to select stably transduced cells following lentiviral infection. For lentivirus production, we transfected lentiviral plasmids with packaging plasmids in 293T cells using polyethylenimine (Sigma-Aldrich, 408727), harvested supernatants containing viral particles 48 and 72 hours later, and filtered through 0.45-μm polyvinylidene difluoride (PVDF) filter before adding to culture of target cells in the presence of polybrene (5 μg/ml; Sigma-Aldrich, H9268). To generate KO cells, the parental cells were infected with LV-gRNA-zeocin vector carrying single gRNAs that target the sequence encoding each gene or empty vector (control) using Lipofectamine 2000 (Invitrogen, 52887) according to the manufacturer's instructions. Forty-eight hours later, the positive cells were selected using zeocin. Sanger sequencing verified mutation in the target sequence in the genes and immunoblot validated loss of the proteins. For experiments in Fig. 1 (F and G), transient transfection was performed using X-tremeGENE DNA transfection reagent (Roche) to generate KO cells. Forty-eight hours after transfection, cells were collected for Western blot analysis. For packaging lentivirus, 293T cells were cotransfected with pMD2.G, pPAX2, and LentiCRISPRv2 constructs using X-tremeGENE DNA transfection reagent (Roche). For infections, cells were incubated with viral supernatants in the presence of polybrene (8 mg/ml); after 48 hours, the infected cells were selected with blasticidin (10 μg/ml) or puromycin (2 μg/ml) for 4 to 6 days before experiments.

Cell proliferation assays

Cells were seeded into a 96-well plate for 200 to 500 cells in 100 μl of medium per well in triplicate for each time point, and their proliferation was measured every 1 or 2 days depending on the growth rate of those cells. There is a tight linear relationship between cell number and the concentration of adenosine 5′-triphosphate (ATP) measured in cell lysate. The bioluminescence-based reagents such as CellTiter-Glo (Promega) can detect ATP, which provides a sensitive readout of cell proliferation. To measure proliferation, 25 μl of CellTiter-Glo was directly added into each well, and the plate was placed on an orbit shaker for gentle rocking to induce cell lysis. Each plate was incubated at room temperature for 10 min to stabilize luminescent signal before it was read using FLUOstar Omega plate reader. Alternatively, MTT assay was performed to measure relative cell viability using (3-[4,5-dimethylthiazol-2-yl]-2,5-diphenyltetrazolium bromide; thiazolyl blue) tetrazolium salt and plate reader. Cells were seeded at 1×10^4 per well in 96-well plates at day 0. At times ranging from 0 to 4 days or 6 days after seeding, MTT was added (10 μl; final concentration of 0.5 mg/ml), and cells were then incubated for 4 hours at 37°C. Optical density measurements were determined with an enzyme-linked immunosorbent assay reader at a wavelength of 590 nm. Background was accounted for by subtracting the value of a vehicle-containing blank from all values. For soft agar assay to measure clonal expansion, cells were seeded at 1×10^4 cells per well in 0.5 ml of growth medium containing 0.35% low melting point agarose (Invitrogen, 16520-100) and seeded on top of a 0.5-ml base layer of medium containing 0.5% agar. The medium was regularly changed every 3 days during the experiments. Colonies were fixed with 10% MeOH and 10% acetic acid at room temperature for 10 min and stained with 1% MeOH, 1% formaldehyde, and 0.05% crystal violet after. Low melting point agarose was premixed with RPMI 2X (Fisher Scientific, SLM202B) complemented with 20% fetal bovine serum, penicillin (200 U/ml), and streptomycin (200 μg/ml). Cells were allowed to grow at 37°C with 5% CO_2 for 3 weeks. Images of wells are acquired using Olympus MVX10 scope, and colonies from the whole field of image were counted using the imaging software NIS-Elements Basic Research (Nikon). All of the cell culture experiments were performed in triplicates and repeated for a minimum of two biological replicates. The cells were treated with doxycycline (Sigma-Aldrich, D9891) during the experiment.

Immunoblot analysis and immunoprecipitation

Cells were lysed in radioimmunoprecipitation assay (RIPA) buffer [50 mM tris-HCl (pH 7.4), 150 mM NaCl, 2 mM EDTA, 1% NP-40, and 0.1% SDS] and sonicated for 20 s at 15% intensity. Generally, 15 to 30 μg of protein lysate were loaded into various percentages of SDS–polyacrylamide gel electrophoresis (SDS-PAGE) in PAGE running buffer [25 mM tris, 192 mM glycine, and 0.1% SDS (pH 8.3)]. Then, proteins were transferred to 0.2 or 0.45 μm of PVDF membrane in transfer buffer (25 mM tris, 192 mM glycine, and 20% methanol). The membranes were blocked by TBST (Tris-buffered saline with 0.1% Tween 20) buffer [150 mM NaCl, 10 mM tris (pH 8.0), and 0.1% Tween 20] supplemented with 5% nonfat milk for 1 hour at room temperature and then blotted with primary antibodies overnight at 4°C on an orbital shaker. After washing five times with

TBST, membranes were incubated with secondary antibodies for 2 hours at room temperature and washed again with TBST five times. The membranes were then either used for ChemiDoc machine (Bio-Rad), developing after incubating with ECL Western Blotting Detection Reagent (Thermo Fisher Scientific, 32106) for 5 min. For immunoprecipitation of protein complexes consisting of EP300/CREBBP-FLAG–tagged M/M fusion peptide, cells were lysed in RIPA buffer [50 mM tris-HCl (pH 8.0), 150 mM NaCl, 0.1% SDS, 0.5% SDC, 1% NP-40, 1X protease inhibitor cocktail, and 1 mM EDTA] and immunoprecipitated with anti-FLAG or anti–immunoglobulin G antibodies in buffer [50 mM tris-HCl (pH 7.5), 150 mM NaCl, 1 mM EDTA, 1 mM EGTA, 1% Triton X-100, 1 mM phenylmethylsulfonyl fluoride, and 1X protease inhibitor cocktail] overnight at 4°C. Protein A/G agarose beads (GenDEPOT, P9203) were then added for 4 hours with agitation at 4°C. Bound proteins were eluted and analyzed by immunoblotting with anti-FLAG, anti-EP300, and anti-CREBBP antibodies.

Peptides, FP assay, and ITC

Human EP300 KIX domain (87 residues spanning from 565-652) and the CREBBP KIX domain (87 residues spanning from 585-672) were expressed using a pMAL-c5E vector. D647A mutant for CREBBP KIX was generated using a site-directed mutagenesis kit (QuickChange XL from Agilent) and expressed in same way as for wild-type CREBBP KIX. M/M (wild-type and mutant) fusion peptides (28 residues from MLL activation domain and 30 residues from MYB activation domain linked by a GG linker) were expressed using a pET-32C vector (fused to thioredoxin). All proteins were expressed in *Escherichia coli* Rosetta (DE3) cells and purified using affinity chromatography followed by anion-exchange chromatography. FP assays were conducted in 96-well Costar black Polystyrene plates (Corning). N-terminally FITC labeled MYB (KEKRIKELELLLMSTENELKGQQAL) and rhodamine-labeled MLL peptides (SDDGNILPSDIMDFVLKNTPSMQAL) were used to detect KIX domain binding via changes in FP. The FP assay mixture was composed of 50 mM Hepes (pH 7.5), 50 mM NaCl, 12 and 45 μM purified EP300 KIX domain or CREBBP KIX domain, respectively (~3× K_d for KIX domain binding to the MYB peptide), 0.5 μM of each fluorescent peptide, and a variable concentration of purified peptide fusion inhibitor to make a total volume of 100 μl per well. After the addition of all assay components, the plates were incubated in the dark for the 30 min at room temperature. The plates were read using a PHERAstar plate reader (BMG Labtech). The FP values as a function of peptide fusion inhibitor concentration were fitted to sigmoidal equation, and IC_{50} values were determined using Origin software. All ITC measurements were performed on the VP-ITC (Microcal, USA) at 25°C. The composition of assay buffer was same [50 mM Hepes and 50 mM NaCl (pH 7.5)] as used for FP assays. The proteins and peptides were dialyzed against the assay buffer and thoroughly degassed before the experiment. The reference cell was filled with water. The KIX domain was then added to the sample cell, and fusion peptide was titrated to KIX from the syringe. Concentration of KIX domain was 20 to 40 μM in all the ITC titrations, whereas concentrations of the ligands were in the range of 400 to 600 μM. Each titration composed of 30 injections always with a 5-μl initial injection (omitted in data fitting) followed by 10-μl subsequent injections. The initial delay was set to 60 s followed by a 180-s delay after each injection. The sample was stirred at 310 rpm, and the reference power was set to 10 μCal/s. The data fitting was done with Microcal Origin software package provided with the instrument.

RNA sequencing and analysis

Sequencing libraries were generated by the Genome Analysis and Technology Core at University of Virginia using oligo(dT)-purified mRNA from 500 ng of total RNA extracted by an RNeasy kit (QIAGEN) and the NEB Next Ultra RNA library preparation kit (New England Biolabs), and 100–base pair single-end sequencing was performed on Illumina NextSeq2000 platform (Illumina). The sequencing data have been deposited to the Gene Expression Omnibus (GEO) Database GSE188705 at www.ncbi.nlm.nih.gov/geo/query/acc.cgi?acc=GSE188705. The sequencing quality was evaluated by FastQC v0.11.8 (available at www.bioinformatics.babraham.ac.uk/projects/fastqc/). The adaptor sequences were trimmed by Trimmomatic v0.39 (*52*). Trimmomatic is a flexible trimmer for Illumina sequence data. The trimmed raw data were mapped to the human reference genome (hh19) by BBMap v38.61 (https://sourceforge.net/projects/bbmap/). The number of fragments that overlaps each gene was assessed by STAR v2.5 (*53*). Transcripts per million (TPM) data were generated by RSEM v1.3.1 (*54*). DEG signatures were generated by comparing TPM levels between the experimental group and the control by limma v3.50 (*55*). Heatmaps were generated by Clustergrammer (*56*). GSEA was performed with the gene expression signature using FGSEA v1.20 (*57*). The gene set signatures were determined by the Molecular Signatures Database v7.4 (*58*).

Statistical analysis

Statistical analyses and graphical presentation were performed with GraphPad Prism 8.2. The results are presented as the mean ± SD and evaluated using an unpaired Student *t* test (two-tailed; $P < 0.05$ was considered to be significant). Kaplan-Meier curves of lung tumor–free survival were generated using Prism 8.2 (log-rank test; $P < 0.05$ was considered to be significant).

SUPPLEMENTARY MATERIALS

Supplementary material for this article is available at https://science.org/doi/10.1126/sciadv.abl4618

View/request a protocol for this paper from *Bio-protocol*.

REFERENCES AND NOTES

1. R. H. Goodman, S. Smolik, CBP/p300 in cell growth, transformation, and development. *Genes Dev.* **14**, 1553–1577 (2000).
2. P. Whyte, N. M. Williamson, E. Harlow, Cellular targets for transformation by the adenovirus E1A proteins. *Cell* **56**, 67–75 (1989).
3. H. Zimmermann, R. Degenkolbe, H. U. Bernard, M. J. O'Connor, The human papillomavirus type 16 E6 oncoprotein can down-regulate p53 activity by targeting the transcriptional coactivator CBP/p300. *J. Virol.* **73**, 6209–6219 (1999).
4. A. Augert, Q. Zhang, B. Bates, M. Cui, X. Wang, G. Wildey, A. Dowlati, D. MacPherson, Small cell lung cancer exhibits frequent inactivating mutations in the histone methyltransferase KMT2D/MLL2: CALGB 151111 (Alliance). *J. Thorac. Oncol.* **12**, 704–713 (2017).
5. J. George, J. S. Lim, S. J. Jang, Y. Cun, L. Ozretic, G. Kong, F. Leenders, X. Lu, L. Fernandez-Cuesta, G. Bosco, C. Muller, I. Dahmen, N. S. Jahchan, K. S. Park, D. Yang, A. N. Karnezis, D. Vaka, A. Torres, M. S. Wang, J. O. Korbel, R. Menon, S. M. Chun, D. Kim, M. Wilkerson, N. Hayes, D. Engelmann, B. Putzer, M. Bos, S. Michels, I. Vlasic, D. Seidel, B. Pinther, P. Schaub, C. Becker, J. Altmuller, J. Yokota, T. Kohno, R. Iwakawa, K. Tsuta, M. Noguchi, T. Muley, H. Hoffmann, P. A. Schnabel, I. Petersen, Y. Chen, A. Soltermann, V. Tischler, C. M. Choi, Y. H. Kim, P. P. Massion, Y. Zou, D. Jovanovic, M. Kontic, G. M. Wright, P. A. Russell, B. Solomon, I. Koch, M. Lindner, L. A. Muscarella, A. la Torre, J. K. Field, M. Jakopovic, J. Knezevic, E. Castanos-Velez, L. Roz, U. Pastorino, O. T. Brustugun, M. Lund-Iversen, E. Thunnissen, J. Kohler, M. Schuler, J. Botling,

M. Sandelin, M. Sanchez-Cespedes, H. B. Salvesen, V. Achter, U. Lang, M. Bogus, P. M. Schneider, T. Zander, S. Ansen, M. Hallek, J. Wolf, M. Vingron, Y. Yatabe, W. D. Travis, P. Nurnberg, C. Reinhardt, S. Perner, L. Heukamp, R. Buttner, S. A. Haas, E. Brambilla, M. Peifer, J. Sage, R. K. Thomas, Comprehensive genomic profiles of small cell lung cancer. *Nature* **524**, 47–53 (2015).

6. M. Peifer, L. Fernandez-Cuesta, M. L. Sos, J. George, D. Seidel, L. H. Kasper, D. Plenker, F. Leenders, R. Sun, T. Zander, R. Menon, M. Koker, I. Dahmen, C. Muller, V. Di Cerbo, H. U. Schildhaus, J. Altmuller, I. Baessmann, C. Becker, B. de Wilde, J. Vandesompele, D. Bohm, S. Ansen, F. Gabler, I. Wilkening, S. Heynck, J. M. Heuckmann, X. Lu, S. L. Carter, K. Cibulskis, S. Banerji, G. Getz, K. S. Park, D. Rauh, C. Grutter, M. Fischer, L. Pasqualucci, G. Wright, Z. Wainer, P. Russell, I. Petersen, Y. Chen, E. Stoelben, C. Ludwig, P. Schnabel, H. Hoffmann, T. Muley, M. Brockmann, W. Engel-Riedel, L. A. Muscarella, V. M. Fazio, H. Groen, W. Timens, H. Sietsma, E. Thunnissen, E. Smit, D. A. Heideman, P. J. Snijders, F. Cappuzzo, C. Ligorio, S. Damiani, J. Field, S. Solberg, O. T. Brustugun, M. Lund-Iversen, J. Sanger, J. H. Clement, A. Soltermann, H. Moch, W. Weder, B. Solomon, J. C. Soria, P. Validire, B. Besse, E. Brambilla, C. Brambilla, S. Lantuejoul, P. Lorimier, P. M. Schneider, M. Hallek, W. Pao, M. Meyerson, J. Sage, J. Shendure, R. Schneider, R. Buttner, J. Wolf, P. Nurnberg, S. Perner, L. C. Heukamp, P. K. Brindle, S. Haas, R. K. Thomas, Integrative genome analyses identify key somatic driver mutations of small-cell lung cancer. *Nat. Genet.* **44**, 1104–1110 (2012).
7. C. M. Rudin, S. Durinck, E. W. Stawiski, J. T. Poirier, Z. Modrusan, D. S. Shames, E. A. Bergbower, Y. Guan, J. Shin, J. Guillory, C. S. Rivers, C. K. Foo, D. Bhatt, J. Stinson, F. Gnad, P. M. Haverty, R. Gentleman, S. Chaudhuri, V. Janakiraman, B. S. Jaiswal, C. Parikh, W. Yuan, Z. Zhang, H. Koeppen, T. D. Wu, H. M. Stern, R. L. Yauch, K. E. Huffman, D. D. Paskulin, P. B. Illei, M. Varella-Garcia, A. F. Gazdar, F. J. de Sauvage, R. Bourgon, J. D. Minna, M. V. Brock, S. Seshagiri, Comprehensive genomic analysis identifies SOX2 as a frequently amplified gene in small-cell lung cancer. *Nat. Genet.* **44**, 1111–1116 (2012).
8. Cancer Genome Atlas Research, Comprehensive molecular characterization of urothelial bladder carcinoma. *Nature* **507**, 315–322 (2014).
9. C. G. Mullighan, J. Zhang, L. H. Kasper, S. Lerach, D. Payne-Turner, L. A. Phillips, S. L. Heatley, L. Holmfeldt, J. R. Collins-Underwood, J. Ma, K. H. Buetow, C. H. Pui, S. D. Baker, P. K. Brindle, J. R. Downing, CREBBP mutations in relapsed acute lymphoblastic leukaemia. *Nature* **471**, 235–239 (2011).
10. L. Pasqualucci, D. Dominguez-Sola, A. Chiarenza, G. Fabbri, A. Grunn, V. Trifonov, L. H. Kasper, S. Lerach, H. Tang, J. Ma, D. Rossi, A. Chadburn, V. V. Murty, C. G. Mullighan, G. Gaidano, R. Rabadan, P. K. Brindle, R. Dalla-Favera, Inactivating mutations of acetyltransferase genes in B-cell lymphoma. *Nature* **471**, 189–195 (2011).
11. S. J. Horton, G. Giotopoulos, H. Yun, S. Vohra, O. Sheppard, R. Bashford-Rogers, M. Rashid, A. Clipson, W. I. Chan, D. Sasca, L. Yiangou, H. Osaki, F. Basheer, P. Gallipoli, N. Burrows, A. Erdem, A. Sybirna, S. Foerster, W. Zhao, T. Sustic, A. P. Harrison, E. Laurenti, J. Okosun, D. Hodson, P. Wright, K. G. Smith, P. Maxwell, J. Fitzgibbon, M. Q. Du, D. J. Adams, B. J. P. Huntly, Early loss of Crebbp confers malignant stem cell properties on lymphoid progenitors. *Nat. Cell Biol.* **19**, 1093–1104 (2017).
12. D. Jia, A. Augert, D. W. Kim, E. Eastwood, N. Wu, A. H. Ibrahim, K. B. Kim, C. T. Dunn, S. P. S. Pillai, A. F. Gazdar, H. Bolouri, K. S. Park, D. MacPherson, CrebbpLoss drives small cell lung cancer and increases sensitivity to HDAC inhibition. *Cancer Discov.* **8**, 1422–1437 (2018).
13. J. Zhang, S. Vlasevska, V. A. Wells, S. Nataraj, A. B. Holmes, R. Duval, S. N. Meyer, T. Mo, K. Basso, P. K. Brindle, S. Hussein, R. Dalla-Favera, L. Pasqualucci, The CREBBP acetyltransferase is a haploinsufficient tumor suppressor in B-cell lymphoma. *Cancer Discov.* **7**, 322–337 (2017).
14. Y. Jiang, A. Ortega-Molina, H. Geng, H. Y. Ying, K. Hatzi, S. Parsa, D. McNally, L. Wang, A. S. Doane, X. Agirre, M. Teater, C. Meydan, Z. Li, D. Poloway, S. Wang, D. Ennishi, D. W. Scott, K. R. Stengel, J. E. Kranz, E. Holson, S. Sharma, J. W. Young, C. S. Chu, R. G. Roeder, R. Shaknovich, S. W. Hiebert, R. D. Gascoyne, W. Tam, O. Elemento, H. G. Wendel, A. M. Melnick, CREBBP inactivation promotes the development of HDAC3-dependent lymphomas. *Cancer Discov.* **7**, 38–53 (2017).
15. N. Attar, S. K. Kurdistani, Exploitation of EP300 and CREBBP lysine acetyltransferases by cancer. *Cold Spring Harb. Perspect. Med.* **7**, a026534 (2017).
16. A. F. Gazdar, P. A. Bunn, J. D. Minna, Small-cell lung cancer: What we know, what we need to know and the path forward. *Nat. Rev. Cancer* **17**, 725–737 (2017).
17. L. H. Kasper, T. Fukuyama, M. A. Biesen, F. Boussouar, C. Tong, A. de Pauw, P. J. Murray, J. M. van Deursen, P. K. Brindle, Conditional knockout mice reveal distinct functions for the global transcriptional coactivators CBP and p300 in T-cell development. *Mol. Cell. Biol.* **26**, 789–809 (2006).
18. G. Mollaoglu, M. R. Guthrie, S. Bohm, J. Bragelmann, I. Can, P. M. Ballieu, A. Marx, J. George, C. Heinen, M. D. Chalishazar, H. Cheng, A. S. Ireland, K. E. Denning, A. Mukhopadhyay, J. M. Vahrenkamp, K. C. Berrett, T. L. Mosbruger, J. Wang, J. L. Kohan, M. E. Salama, B. L. Witt, M. Peifer, R. K. Thomas, J. Gertz, J. E. Johnson, A. F. Gazdar, R. J. Wechsler-Reya, M. L. Sos, T. G. Oliver, MYC drives progression of small cell lung cancer to a variant neuroendocrine subtype with vulnerability to aurora kinase inhibition. *Cancer Cell* **31**, 270–285 (2017).
19. C. M. Rudin, J. T. Poirier, L. A. Byers, C. Dive, A. Dowlati, J. George, J. V. Heymach, J. E. Johnson, J. M. Lehman, D. MacPherson, P. P. Massion, J. D. Minna, T. G. Oliver, V. Quaranta, J. Sage, R. K. Thomas, C. R. Vakoc, A. F. Gazdar, Molecular subtypes of small cell lung cancer: A synthesis of human and mouse model data. *Nat. Rev. Cancer* **19**, 289–297 (2019).
20. B. E. Schaffer, K. S. Park, G. Yiu, J. F. Conklin, C. Lin, D. L. Burkhart, A. N. Karnezis, E. A. Sweet-Cordero, J. Sage, Loss of p130 accelerates tumor development in a mouse model for human small-cell lung carcinoma. *Cancer Res.* **70**, 3877–3883 (2010).
21. K. D. Sutherland, N. Proost, I. Brouns, D. Adriaensen, J. Y. Song, A. Berns, Cell of origin of small cell lung cancer: Inactivation of Trp53 and Rb1 in distinct cell types of adult mouse lung. *Cancer Cell* **19**, 754–764 (2011).
22. D. W. Kim, N. Wu, Y. C. Kim, P. F. Cheng, R. Basom, D. Kim, C. T. Dunn, A. Y. Lee, K. Kim, C. S. Lee, A. Singh, A. F. Gazdar, C. R. Harris, R. N. Eisenman, K. S. Park, D. MacPherson, Genetic requirement for Mycl and efficacy of RNA Pol I inhibition in mouse models of small cell lung cancer. *Genes Dev.* **30**, 1289–1299 (2016).
23. E. M. Bowers, G. Yan, C. Mukherjee, A. Orry, L. Wang, M. A. Holbert, N. T. Crump, C. A. Hazzalin, G. Liszczak, H. Yuan, C. Larocca, S. A. Saldanha, R. Abagyan, Y. Sun, D. J. Meyers, R. Marmorstein, L. C. Mahadevan, R. M. Alani, P. A. Cole, Virtual ligand screening of the p300/CBP histone acetyltransferase: Identification of a selective small molecule inhibitor. *Chem. Biol.* **17**, 471–482 (2010).
24. A. Hammitzsch, C. Tallant, O. Fedorov, A. O'Mahony, P. E. Brennan, D. A. Hay, F. O. Martinez, M. H. Al-Mossawi, J. de Wit, M. Vecellio, C. Wells, P. Wordsworth, S. Muller, S. Knapp, P. Bowness, CBP30, a selective CBP/p300 bromodomain inhibitor, suppresses human Th17 responses. *Proc. Natl. Acad. Sci. U.S.A.* **112**, 10768–10773 (2015).
25. S. Picaud, O. Fedorov, A. Thanasopoulou, K. Leonards, K. Jones, J. Meier, H. Olzscha, O. Monteiro, S. Martin, M. Philpott, A. Tumber, P. Filippakopoulos, C. Yapp, C. Wells, K. H. Che, A. Bannister, S. Robson, U. Kumar, N. Parr, K. Lee, D. Lugo, P. Jeffrey, S. Taylor, M. L. Vecellio, C. Bountra, P. E. Brennan, A. O'Mahony, S. Velichko, S. Muller, D. Hay, D. L. Daniels, M. Urh, N. B. La Thangue, T. Kouzarides, R. Prinjha, J. Schwaller, S. Knapp, Generation of a selective small molecule inhibitor of the CBP/p300 bromodomain for leukemia therapy. *Cancer Res.* **75**, 5106–5119 (2015).
26. H. Ogiwara, M. Sasaki, T. Mitachi, T. Oike, S. Higuchi, Y. Tominaga, T. Kohno, Targeting p300 addiction in CBP-deficient cancers causes synthetic lethality by apoptotic cell death due to abrogation of MYC expression. *Cancer Discov.* **6**, 430–445 (2016).
27. H. M. Chan, N. B. La Thangue, p300/CBP proteins: HATs for transcriptional bridges and scaffolds. *J. Cell Sci.* **114**, 2363–2373 (2001).
28. D. E. Scott, A. G. Coyne, S. A. Hudson, C. Abell, Fragment-based approaches in drug discovery and chemical biology. *Biochemistry* **51**, 4990–5003 (2012).
29. R. N. De Guzman, N. K. Goto, H. J. Dyson, P. E. Wright, Structural basis for cooperative transcription factor binding to the CBP coactivator. *J. Mol. Biol.* **355**, 1005–1013 (2006).
30. S. Jin, H. Zhao, Y. Yi, Y. Nakata, A. Kalota, A. M. Gewirtz, c-Myb binds MLL through menin in human leukemia cells and is an important driver of MLL-associated leukemogenesis. *J. Clin. Invest.* **120**, 593–606 (2010).
31. S. T. Joy, M. J. Henley, S. N. De Salle, M. S. Beyersdorf, I. W. Vock, A. J. L. Huldin, A. K. Mapp, A dual-site inhibitor of CBP/p300 KIX is a selective and effective modulator of Myb. *J. Am. Chem. Soc.* **143**, 15056–15062 (2021).
32. J. L. Best, C. A. Amezcua, B. Mayr, L. Flechner, C. M. Murawsky, B. Emerson, T. Zor, K. H. Gardner, M. Montminy, Identification of small-molecule antagonists that inhibit an activator: Coactivator interaction. *Proc. Natl. Acad. Sci. U.S.A.* **101**, 17622–17627 (2004).
33. F. Xie, B. X. Li, A. Kassenbrock, C. Xue, X. Wang, D. Z. Qian, R. C. Sears, X. Xiao, Identification of a potent inhibitor of CREB-mediated gene transcription with efficacious in vivo anticancer activity. *J. Med. Chem.* **58**, 5075–5087 (2015).
34. B. X. Li, R. Gardner, C. Xue, D. Z. Qian, F. Xie, G. Thomas, S. C. Kazmierczak, B. A. Habecker, X. Xiao, Systemic inhibition of CREB is well-tolerated in vivo. *Sci. Rep.* **6**, 34513 (2016).
35. L. M. Lasko, C. G. Jakob, R. P. Edalji, W. Qiu, D. Montgomery, E. L. Digiammarino, T. M. Hansen, R. M. Risi, R. Frey, V. Manaves, B. Shaw, M. Algire, P. Hessler, L. T. Lam, T. Uziel, E. Faivre, D. Ferguson, F. G. Buchanan, R. L. Martin, M. Torrent, G. G. Chiang, K. Karukurichi, J. W. Langston, B. T. Weinert, C. Choudhary, P. de Vries, J. H. Van Drie, D. McElligott, E. Kesicki, R. Marmorstein, C. Sun, P. A. Cole, S. H. Rosenberg, M. R. Michaelides, A. Lai, K. D. Bromberg, Discovery of a selective catalytic p300/CBP inhibitor that targets lineage-specific tumours. *Nature* **550**, 128–132 (2017).
36. S. N. Meyer, C. Scuoppo, S. Vlasevska, E. Bal, A. B. Holmes, M. Holloman, L. Garcia-Ibanez, S. Nataraj, R. Duval, T. Vantrimpont, K. Basso, N. Brooks, R. Dalla-Favera, L. Pasqualucci, Unique and shared epigenetic programs of the CREBBP and EP300 acetyltransferases in germinal center B cells reveal targetable dependencies in lymphoma. *Immunity* **51**, 535–547.e9 (2019).
37. Z. Arany, D. Newsome, E. Oldread, D. M. Livingston, R. Eckner, A family of transcriptional adaptor proteins targeted by the E1A oncoprotein. *Nature* **374**, 81–84 (1995).
38. J. S. Lee, X. Zhang, Y. Shi, Differential interactions of the CREB/ATF family of transcription factors with p300 and adenovirus E1A. *J. Biol. Chem.* **271**, 17666–17674 (1996).
39. E. Kalkhoven, CBP and p300: HATs for different occasions. *Biochem. Pharmacol.* **68**, 1145–1155 (2004).

40. A. L. Kung, V. I. Rebel, R. T. Bronson, L. E. Ch'ng, C. A. Sieff, D. M. Livingston, T. P. Yao, Gene dose-dependent control of hematopoiesis and hematologic tumor suppression by CBP. *Genes Dev.* **14**, 272–277 (2000).
41. V. I. Rebel, A. L. Kung, E. A. Tanner, H. Yang, R. T. Bronson, D. M. Livingston, Distinct roles for CREB-binding protein and p300 in hematopoietic stem cell self-renewal. *Proc. Natl. Acad. Sci. U.S.A.* **99**, 14789–14794 (2002).
42. J. F. Roth, N. Shikama, C. Henzen, I. Desbaillets, W. Lutz, S. Marino, J. Wittwer, H. Schorle, M. Gassmann, R. Eckner, Differential role of p300 and CBP acetyltransferase during myogenesis: p300 acts upstream of MyoD and Myf5. *EMBO J.* **22**, 5186–5196 (2003).
43. N. Shikama, W. Lutz, R. Kretzschmar, N. Sauter, J. F. Roth, S. Marino, J. Wittwer, A. Scheidweiler, R. Eckner, Essential function of p300 acetyltransferase activity in heart, lung and small intestine formation. *EMBO J.* **22**, 5175–5185 (2003).
44. Y. Tanaka, I. Naruse, T. Maekawa, H. Masuya, T. Shiroishi, S. Ishii, Abnormal skeletal patterning in embryos lacking a single Cbp allele: A partial similarity with Rubinstein-Taybi syndrome. *Proc. Natl. Acad. Sci. U.S.A.* **94**, 10215–10220 (1997).
45. T. P. Yao, S. P. Oh, M. Fuchs, N. D. Zhou, L. E. Ch'ng, D. Newsome, R. T. Bronson, E. Li, D. M. Livingston, R. Eckner, Gene dosage-dependent embryonic development and proliferation defects in mice lacking the transcriptional integrator p300. *Cell* **93**, 361–372 (1998).
46. L. H. Kasper, F. Boussouar, P. A. Ney, C. W. Jackson, J. Rehg, J. M. van Deursen, P. K. Brindle, A transcription-factor-binding surface of coactivator p300 is required for haematopoiesis. *Nature* **419**, 738–743 (2002).
47. E. L. Jackson, N. Willis, K. Mercer, R. T. Bronson, D. Crowley, R. Montoya, T. Jacks, D. A. Tuveson, Analysis of lung tumor initiation and progression using conditional expression of oncogenic K-ras. *Genes Dev.* **15**, 3243–3248 (2001).
48. D. MacPherson, K. Conkrite, M. Tam, S. Mukai, D. Mu, T. Jacks, Murine bilateral retinoblastoma exhibiting rapid-onset, metastatic progression and N-myc gene amplification. *EMBO J.* **26**, 784–794 (2007).
49. S. Marino, M. Vooijs, H. van Der Gulden, J. Jonkers, A. Berns, Induction of medulloblastomas in p53-null mutant mice by somatic inactivation of Rb in the external granular layer cells of the cerebellum. *Genes Dev.* **14**, 994–1004 (2000).
50. J. Sage, A. L. Miller, P. A. Perez-Mancera, J. M. Wysocki, T. Jacks, Acute mutation of retinoblastoma gene function is sufficient for cell cycle re-entry. *Nature* **424**, 223–228 (2003).
51. M. DuPage, A. L. Dooley, T. Jacks, Conditional mouse lung cancer models using adenoviral or lentiviral delivery of Cre recombinase. *Nat. Protoc.* **4**, 1064–1072 (2009).
52. A. M. Bolger, M. Lohse, B. Usadel, Trimmomatic: A flexible trimmer for Illumina sequence data. *Bioinformatics* **30**, 2114–2120 (2014).
53. A. Dobin, C. A. Davis, F. Schlesinger, J. Drenkow, C. Zaleski, S. Jha, P. Batut, M. Chaisson, T. R. Gingeras, STAR: Ultrafast universal RNA-seq aligner. *Bioinformatics* **29**, 15–21 (2013).
54. B. Li, C. N. Dewey, RSEM: Accurate transcript quantification from RNA-Seq data with or without a reference genome. *BMC Bioinformatics* **12**, 323 (2011).
55. M. E. Ritchie, B. Phipson, D. Wu, Y. Hu, C. W. Law, W. Shi, G. K. Smyth, *limma* powers differential expression analyses for RNA-sequencing and microarray studies. *Nucleic Acids Res.* **43**, e47 (2015).
56. N. F. Fernandez, G. W. Gundersen, A. Rahman, M. L. Grimes, K. Rikova, P. Hornbeck, A. Ma'ayan, Clustergrammer, a web-based heatmap visualization and analysis tool for high-dimensional biological data. *Sci. Data* **4**, 170151 (2017).
57. G. Korotkevich, V. Sukhov, N. Budin, B. Shpak, M. N. Artyomov, A. Sergushichev, Fast gene set enrichment analysis. *bioRxiv*, 060012 (2019).
58. A. Subramanian, P. Tamayo, V. K. Mootha, S. Mukherjee, B. L. Ebert, M. A. Gillette, A. Paulovich, S. L. Pomeroy, T. R. Golub, E. S. Lander, J. P. Mesirov, Gene set enrichment analysis: A knowledge-based approach for interpreting genome-wide expression profiles. *Proc. Natl. Acad. Sci. U.S.A.* **102**, 15545–15550 (2005).

Acknowledgments: For the data of MSK-IMPACT Clinical Cohort Sequencing from cBioportal, we are grateful to the members of the Molecular Diagnostics Service in the Department of Pathology funded, in part, by the Marie-Josée and Henry R. Kravis Center for Molecular Oncology and the MSK Cancer Center Core. We thank J. Hsu, J. Sage, and H. Agaisse for reading the manuscript. We also thank C. Sonnet in Vector Development Laboratory at Baylor College of Medicine for the service of generating adenovirus CRISPR-Cre hybrid vector. **Funding:** This work is supported by National Institutes of Health grants R01CA194461 (to K.-S.P.), U01CA224293 (to K.-S.P.), R01GM100776 (to T.P.B.), R56AI108767 (to T.P.B.), R01CA204020 (to X.S.), P30CA044579 (UVA Cancer Center), and P30CA008748 (MSK Cancer Center); University of Virginia 3Cavalier grant (to K.-S.P. and J.H.B.); and Adenoid Cystic Carcinoma Research Foundation grant (to J.H.B.). **Author contributions:** Conceptualization: K.-B.K., X.S., T.P.B., J.H.B., and K.-S.P. Methodology: K.-B.K., A.K., Y.X., D.-W.K., Y.H., P.-C.H., Y.Z., and L.J.M. Investigation: K.-B.K., A.K., K.-S.P., and J.H.B. Visualization: K.-B.K., A.K., and K.-S.P. Supervision: J.-I.P., X.S., J.H.B., and K.-S.P. Writing—original draft: K.-B.K., T.P.B., J.H.B., and K.-S.P. Writing—review and editing: K.-B.K., A.K., T.P.B., J.H.B., and K.-SP. **Competing interests:** The authors declare that they have no competing interests. **Data and materials availability:** All data needed to evaluate the conclusions in the paper are present in the paper and/or the Supplementary Materials. The RNA sequencing data have been posited to NCBI GEO Datasets (GEO Database GSE188705).

Submitted 30 July 2021
Accepted 23 December 2021
Published 16 February 2022
10.1126/sciadv.abl4618